NASA-CR-195237

NASA
IN-46-CR
209498
P 80

Analysis of EUV/FUV Dayglow and Auroral Measurements

Final Report

Contract No. NASW-4744

Prepared for:

NASA Headquarters
Washington, DC 20546

Prepared by:

T. Majeed, D. J. Strickland, and R. Link

Computational Physics, Inc.
2750 Prosperity Ave.
Suite 600
Fairfax, VA 22031

(NASA-CR-195237) ANALYSIS OF EUV/FUV DAYGLOW AND AURORAL MEASUREMENTS Final Report (Computational Physics) 80 p

N94-27393

Unclas

G3/46 0209498

January, 1994

Analysis of EUV/FUV Dayglow and Auroral Measurements

Final Report

Contract No. NASW-4744

Prepared for:

NASA Headquarters
Washington, DC 20546

Prepared by:

T. Majeed, D. J. Strickland, and R. Link

Computational Physics, Inc.
2750 Prosperity Ave.
Suite 600
Fairfax, VA 22031

January, 1994

TABLE OF CONTENTS

1. INTRODUCTION ..... p. 1

2. ORIGINAL AND MODIFIED ANALYSIS APPROACH ..... p. 4

3. STP 78-1 DATA REDUCTION ..... p. 6

3.1 Request for STP 78-1 data ..... p. 6
3.2 Transfer of STP 78-1 data to CPI's computer system ..... p. 7
3.3 Data Reduction ..... p. 7

4. RESULTS ..... p. 11

4.1 Averaged data versus time ..... p. 11
4.2 Selected oval averaged spectra ..... p. 17

5. DISCUSSION AND CONCLUSIONS ..... p. 20

6. REFERENCES ..... p. 21

APPENDIX A ..... p. A1

APPENDIX B ..... p. B1

FIGURES

Figure 1. Three hour geomagnetic index a_p from 3/19/79 (day 78) through 3/29 (day 88). The vertical broken lines denote times for which data have been analyzed in this work ..... p. 7

Figure 2. Latitude of look vector at an altitude of 130 km versus time and latitude of satellite as STP 78-1 crossed the northern auroral oval on Pass 391. A given point in the figure refers to the measurement of a single spectrum. The points within each vertical grouping (8 or 9) refer to a single precession of the look vector and correspond to viewing angles from 120° to 150° (nadir is 180°; the most nadir angle achievable within the viewing cone is 150°). Because of a low signal to noise ratio, the 8 or 9 spectra per precession at viewing angles $\geq$ 120° have been summed. In spite of the fact that a single latitude can be effectively assigned to the *location* of the satellite during the partial precession under discussion, ~10° of latitude are seen by the spectrometer during this time. Thus, the effective field-of-view is on the same scale as the width of the auroral oval from its low latitude to its high latitude boundary ..... p. 9

Figure 3. Nadir OI 98.9 nm versus time on Day 79, 1979 showing dayglow and auroral emission. Each data point was obtained by averaging the eight or nine spectra per precession that were recorded for look angles greater than 120° (see Figure 2 for further information concerning this averaging procedure). OI 98.9 nm was selected for this and the subsequent four figures because it is one of the brightest features within the wavelength range of the instrument. The values below the UT scale provide solar zenith angle at the satellite and satellite location in geographic and geomagnetic coordinates. The designator N within the figure identifies the location of the northern auroral oval on the dayside. The designators S identify the locations of the southern auroral oval on the nightside for electron and proton aurora, respectively. The proton aurora was identified from enhancements in HI 121.6 nm above the geocorona background level. Similar enhancements were not seen in the other data being addressed in this report ..... p. 12

Figure 4. Similar to Figure 3 except for Day 80. The upper panel shows weak auroral emission near 16800 s with structure near 16000 s which is contaminated signal due to energetic particles entering the instrument as the satellite passed through the south Atlantic Anomaly (SAA in figure). The lower panel begins where the upper panels stops and identifies the southern auroral oval on the dayside and the northern auroral oval on the day and nightsides ..... p. 13

Figure 5. Similar to Figure 4 except later on Day 80 ..... p. 14

Figure 6. Similar to Figure 4 except on Day 81. Dayside and nightside aurora are prominent in these data ..... p. 15

Figure 7. Similar to Figure 4 except on Days 85 and 86 ..... p. 16

Figure 8. Average spectra for the electron and proton aurora identified in Figure 3. See Table 2 for identification of the brighter features ..... p. 18

Figure 9. Average spectra for the northern auroral oval on the nightside identified in the upper panel of Figure 5 and for the southern auroral oval, also on the nightside identified in the lower panel ..... p. 18

Figure 10. Average spectra for the three nightside auroras identified in Figure 6 ..... p. 19

Figure 11. Average spectra for the three dayside auroras identified in Figure 6..... p. 19

TABLES

Table 1. Dates and time intervals for which data have been reduced and analyzed in this work.....p. 6

Table 2. Key emission features appearing within the observed spectral range. Species, transition, wavelength channels, and nearby channel used for background subtracted are included for each feature.....p. 8

1. INTRODUCTION

This report documents investigations carried out over the twelve month period-of-performance on Contract NASW-4744 which commenced in November, 1992. Dr. Richard Link served as PI until July at which time he joined Southwest Research Institute. In July, Computational Physics, Inc. (CPI) requested that Dr. Tariq Majeed become PI and coordinate the remaining work with Dr. Douglas Strickland. The requested change was subsequently approved by NASA. The contract identifies the following three tasks:

1. Analysis of the OII 83.4 nm dayglow and comparison with incoherent scatter radar data
2. Analysis of the EUV spectrum of an electron aurora
3. Analysis of the EUV spectrum of a proton-hydrogen-electron aurora.

Dr. Link performed work on the first task. The appendices contain preprints of two papers written by Dr. Link under this first task.. Paper 1 examines the effect of new $O(^3P)$ photoionization cross sections, N_2 photoabsorption cross sections, and O^+ oscillator strengths and transition probabilities on the OII 83.4 nm dayglow. Calculated 83.4 nm intensities using the new parameters are in good agreement with rocket measurements and do not support a suggested reduction in the N_2 photoabsorption cross section from an earlier analysis. Paper 2 addresses the problem of remote sensing the dayside F2 region using limb OII 83.4 nm data. The conclusion based on selected calculations of the limb 83.4 nm intensity is that estimates of N_mF2 (electron density at F2 peak) and h_mF2 (height of the peak) can be in error by at least a factor of two and 50 km, respectively.

Drs. Majeed and Strickland worked on the auroral tasks which were directed toward an analysis of data from the U.C. Berkeley experiment on-board satellite STP 78-1 (Bowyer et al., 1981). The main body of this report documents the work of Majeed and Strickland.

We would like to acknowledge Dr. Robert McCoy of the Naval Research Laboratory for providing us with STP 78-1 data. A request for data was first made to Dr. Supriya Chakrabarti of Boston University. Dr. McCoy was contacted after it became apparent that data would not arrive in time from Dr. Chakrabarti to perform an analysis before the end of this contract. Data were provided by Dr. McCoy that span a two week period starting on 3/11/79. During this period, an intense geomagnetic storm occurred on 3/22. Unfortunately, the files containing data for this storm were not located until the end of this contract. Thus, the analysis to follow addresses other data during the available period under less disturbed conditions.

An important observation will be discussed which limits the usefulness of the Berkeley data for auroral investigations. The observation relates to the field-of-view (FOV) which precesses about a horizontal axis perpendicular to the plane of the orbit. The look vector sweeps out a cone whose extreme zenith angle is 150°. Analysis papers such as Chakrabarti (1985) present plots of nadir viewing auroral data versus the latitude of the satellite. Such data have been summed over several degrees of precession centered about 150°. Typically, a second sum has been performed over several consecutive precessions of the individual summed nadir values. Thus, an individual data point corresponds to emission from several degrees of latitude. For summing ±30° about 150°, emission is recorded over approximately 10° of latitude.

The Berkeley instrument is a spectrometer which measures emission from 500 to 1400 Å at a resolution of 8 Å in its EUV/FUV mode. The data to be addressed in this report were collected in this mode. It is necessary to sum spectra as described above since an individual spectrum contains few counts at most of its wavelengths. Typically, a wide range of auroral conditions exists over the latitudinal range covered by the summed data. Furthermore, there is considerable overlap in the effective FOV of the summed data from data point to data point when these points are separated by a few degrees of latitude or less (as is the case in papers that have addressed the Berkeley data). The best that one can do in terms of quantitative analysis is to produce a single summed spectrum across the auroral oval and compare it with similar spectra for other oval crossings. There may be changes in spectral shape with changes in the mean energy of the precipitating particles and in composition from one oval crossing to another. It is questionable, however, whether meaningful interpretation can be given to spectral changes given the extreme spatial averaging and the need to untangle composition from precipitation effects.

To our knowledge, no one has addressed the above issue in any paper or report discussing the STP 78-1 Berkeley auroral data. Its relevance relates to the fact that analysts within the auroral/aeronomy community continue to work with the data. This contract has given us the opportunity to gain the insights discussed above. Although the insights have a negative impact on the usability of the above data, they serve a useful purpose in alerting analysts who are unfamiliar with the limitations imposed by the need to sum the data. In spite of these limitations, we will present a brief description of the analysis conducted under this contract, with emphasis on comparing average spectral behavior from one oval crossing to another. The findings are uninteresting given the unavoidable limitation imposed upon us of working with only quiet time auroral data for which the oval averaged spectral shape was similar among the available data sets. One exception is the distinct difference in NII 108.5 nm between a proton and an electron event

for approximately the same energy inputs. The difference is likely related to the high excitation threshold (35 eV). We conclude that excitation by secondary electrons is unimportant for the proton event and that the cross sections for production of 108.5 nm by proton and H atom impact have significantly smaller maxima than the corresponding cross section for electron impact.

2. ORIGINAL AND MODIFIED ANALYSIS PLANS

The following list identifies the steps that were to be taken in our original approach to analysis of the STP 78-1 auroral data.

- develop software to conveniently display data versus time and wavelength
- conduct data survey
- select times at which spectral data had good counting statistics
- minimize summing of spectra in order to examine their evolution across the oval and from one oval crossing to another
- review literature on electron impact cross sections associated with observed O, O^+, N, and N^+ emissions
- run CPI's auroral electron transport model to obtain emission yield curves vs. characteristic energy for precipitating electron spectra characterized by Gaussian and Maxwellian distributions. Do this for one or more MSIS model atmospheres
- interpret changes in the shape of the spectral data in terms of changes in composition changes (O/N2 and N/N2) and changes in the hardness of the precipitating electron spectrum

We modified this approach after performing simple geometrical calculations to determine the effective FOV of the Berkeley spectrometer while recording auroral emission below the satellite. As noted in the introduction, this FOV for a *single precession* is on the order of 10^o in latitude due to the need to sum spectra. Without summing, the signal-to-noise is too small to characterize the emission. Consequently, a display of the data versus the latitude of the satellite does not show localized emission at a given latitude. Such a display gives a running average with the averaging width on the order of the width of the auroral oval. This condition severely limits the amount of quantitative information that can be obtained from the Berkeley auroral data due to the aurora being highly structured along the satellite path. The following list identifies the steps that were actually taken in our analysis.

- develop software to conveniently display data versus time and wavelength
- investigate viewing geometry
- conduct data survey
- produce single summed nadir spectrum over full width of oval
- compare selected oval averaged spectra.

Since useful information cannot be obtained from one point to another during a crossing of the auroral oval, we have produced oval averaged spectra and then made comparisons among them. It is pointless to use yield curves as identified above for determining spectral properties of the precipitation since the effective FOV corresponds to a region over which there will be a wide range of precipitation characteristics. Thus, the final step, as shown above, is to simply compare oval averaged spectra which will be discussed in Section 4.

3. STP 78-1 DATA REDUCTION

The spectrometer recorded the raw data in counts every 0.2 second interval in its 128 wavelength channels (50-140 nm) from an altitude of 600 km. The satellite was placed in a circular polar orbit lying in the noon-midnight meridian, precessing at about 1° per day to maintain a sun-synchronous orbit. The satellites spun at a rate of one precession every four seconds with its spin axis perpendicular to the orbital plane. The spectrometer's line-of-sight swept out a 60° cone about this spin axis. The motion thus placed the look vector within 30° of zenith (nadir) at the top (bottom) of the cone. In the discussion to follow, we will reference the look vector by zenith angle. The range of angles to be considered in this work is 120° to 150°.

3.1 Request for STP 78-1 data

Dr. Supriya Chakrabarti of Boston University was first contacted to provide us with STP 78-1 emission data. We then contacted Dr. Robert McCoy of the Naval Research Laboratory who possessed data for approximately two weeks of observations from March 11 to March 26, 1979 and agreed to make the data available to us. During this period, an intense geomagnetic storm occurred on March 22, 1979 (39000 to 52000 s UT) (see, e.g., McPherron and Manka, 1985 for a discussion of this storm). The occurrence of this storm can be seen in Figure 1 where the three hour geomagnetic index, a_p exceeded 100. Unfortunately, the files containing auroral data for this storm could not be located in time for analysis under this contract. Table 1 identifies the time intervals for which data were reduced and displayed. These intervals can be seen in Figure 1 as vertical broken lines. As will be shown shortly, aurora were observed on several crossings of the northern and southern auroral oval, although much less intense than during the storm (based on our opportunity to finally examine storm data at the end of the contract period).

Date	Starting time (UT)	Ending time (UT)	Polar passes
79079	59690	71925	1
79080	7162	36500	4
79081	29607	38435	1
79085	78631	86300	1.5
79086	4000	7600	1

Table 1. Dates and time intervals for which data have been reduced and analyzed in this work.

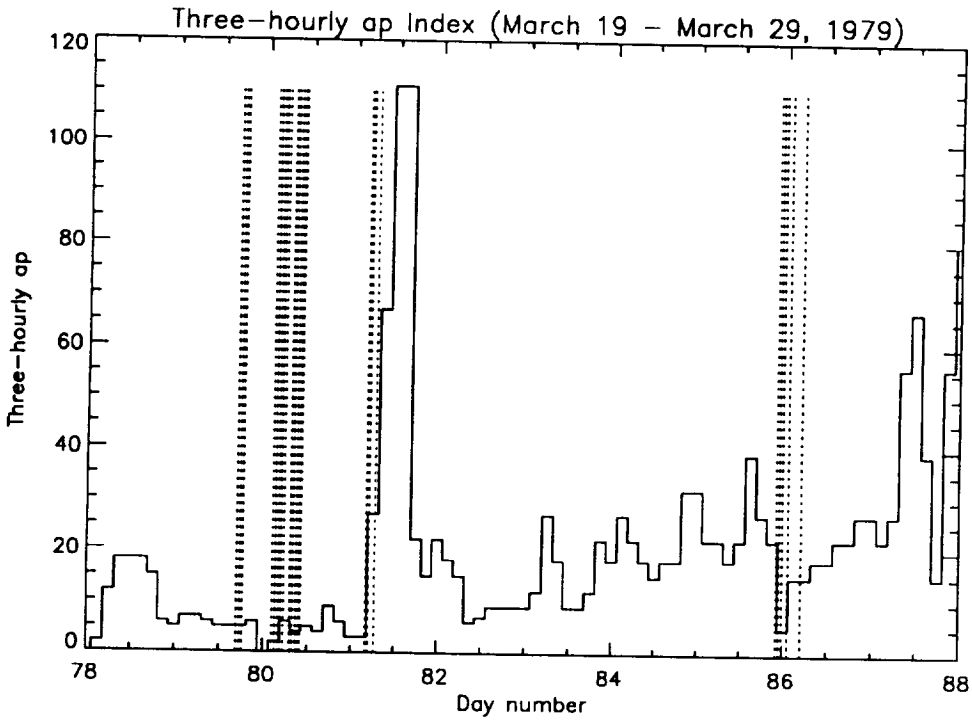

Figure 1. Three hour geomagnetic index a_p from 3/19/79 (day 78) through 3/29 (day 88). The vertical broken lines denote times for which data have been analyzed in this work.

3.2 Transfer of STP 78-1 data to CPI's computer system

Emission data at NRL were stored in several files. Each data file was associated with an aspect file which contained information on satellite attitude, time, latitude, longitude, and viewing direction. Both data and aspect files were transferred from NRL to CPI's computer system by using the File Transfer Protocol (FTP) facility provided by our UNIX and VMS systems.

3.3 Data Reduction

3.3.1 Time profiles of nadir data

Various routines in IDL were developed to handle the data. The routine READSATDATA was used to extract and calibrate the raw data as a function of time for designated emission features. Table 2 identifies the stronger features present in the observed spectra along with their associated wavelength channels and channels used to determine

background counts due to scattering off the grating. After subtraction of the background, the data were calibrated in Rayleighs/bin and output to a file. Each data point referred to a single measurement as the line-of-sight precessed within the above described 60° cone.

Emission Feature (nm)	Species	Transition	WL channels	BG Channel
OII 83.4	O^+	$4P \leftarrow {}^4S^0$	15 - 17	18
OI 98.9	O	${}^3P \leftarrow {}^3D^\circ$	42 - 44	40
OI 102.7	O	$2P^4 \leftarrow 4S^\circ$	49 - 51	48
NII 108.5	N^+	${}^3P \leftarrow {}^3D^\circ$	61 - 63	63
NI 113.4	N	$4S^0 \leftarrow 4P$	69 - 71	68
NI 116.8	N	${}^2D^\circ \leftarrow {}^2P$	76 - 78	75
HI 121.6	H	${}^2S \leftarrow {}^2P^0$	85 - 87	89
OI 130.4	O	${}^3P \leftarrow {}^3S^\circ$	102 - 104	106
OI 135.6	O	${}^3P \leftarrow {}^5S^0$	111 - 113	114

Table 2. Key emission features appearing within the observed spectral range. Species, transition, wavelength channels, and nearby channel used for background subtracted are included for each feature.

Averaging of the data over look angle was required due to poor counting statistics for a single data point. Routine PRESSORT was written to perform the averaging. Figure 2 shows the angular separation (degrees of latitude between adjacent look vectors at a pierce-point altitude of 130 km along the adjacent lines-of-sight) between data points for near-nadir viewing as the satellite passed through the northern auroral oval on Pass 391 of Day 81. A given near-vertical distribution of points (eight or nine) refers to individual measurements within a given precession for all zenith viewing angles greater than 120°. An average over the points falling within the interval from 120° to 150° (most nadir angle available) was performed by PRESSORT for the data to follow. It is significant that an averaged value corresponds to about 10° of latitude. The distribution of points in the figure shows that significant overlap in latitude occurs from one averaged value to the next. The averaged data thus represent a running average with nearly the same information in adjacent points and with an effective FOV comparable to the width of the auroral oval. We regard Figure 2 as the most important figure in this report whose interpretation

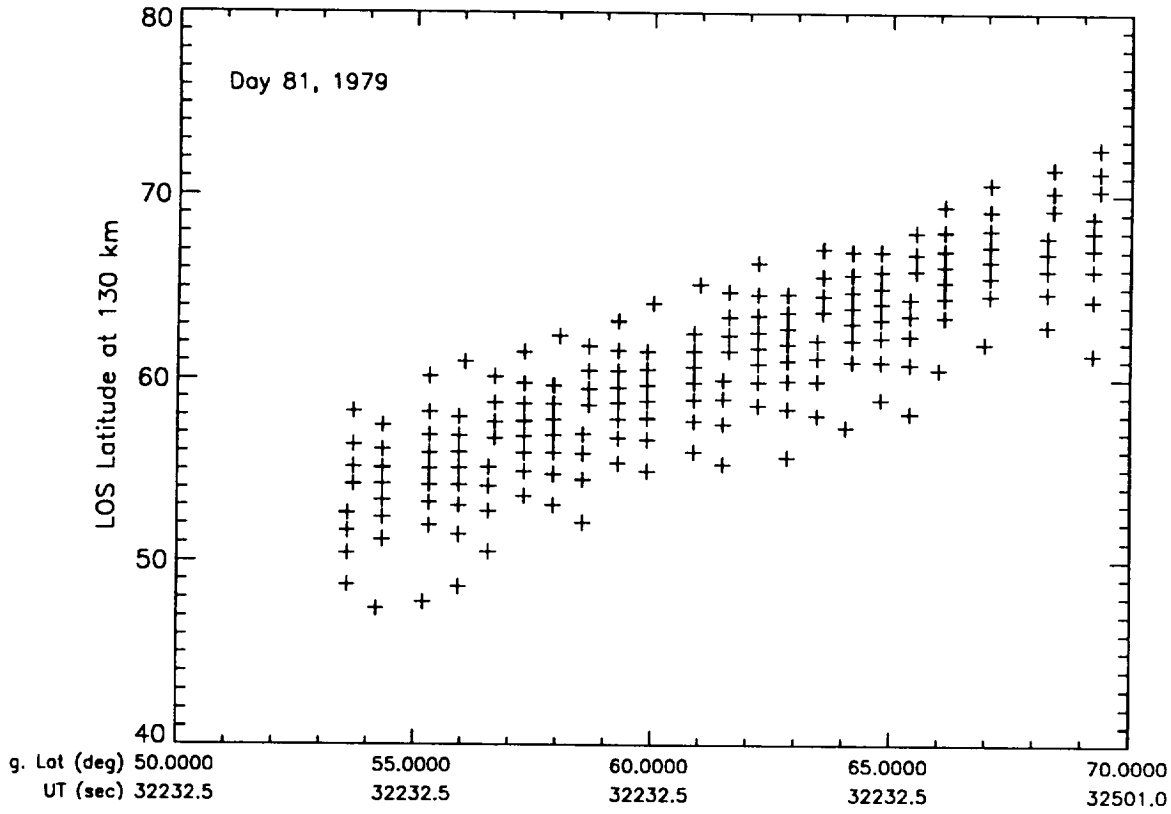

Figure 2. Latitude of look vector at an altitude of 130 km versus time and latitude of satellite as STP 78-1 crossed the northern auroral oval on Pass 391. A given point in the figure refers to the measurement of a single spectrum. The points within each vertical grouping (8 or 9) refer to a single precession of the look vector and correspond to viewing angles from 120° to 150° (nadir is 180°; the most nadir angle achievable within the viewing cone is 150°). Because of a low signal to noise ratio, the 8 or 9 spectra per precession at viewing angles $\geq$ 120° have been summed. In spite of the fact that a single latitude can be effectively assigned to the *location* of the satellite during the partial precession under discussion, ~10° of latitude are seen by the spectrometer during this time. Thus, the effective field-of-view is on the same scale as the width of the auroral oval from its low latitude to its high latitude boundary.

leads to the conclusion that STP 78-1 auroral data are of very limited use for quantitative analysis due to the presence of significant spatial structure over the FOV associated with the averaging process.

Due to poor counting statistics even after the above averaging process, further averaging was done using routine BINSORT. This routine generated averages over 20 precessions which will be presented in the next section in the form of OI 98.9 nm intensity versus time for several crossings of the northern and southern auroral ovals.

3.3.2 Auroral Spectra

A routine named READSATSPEC was written to produce a radiance spectrum in Rayleighs/bin for a single precession averaged over the eight or nine available spectra for zenith angles greater than 120°. The output of this routine is a set of such spectra for a selected interval of time. The interval of interest here is 200 s which is the approximate time during which auroral oval emission is seen in the precession averaged data. Fifty spectra are thus output from READSATSPEC for those crossing of the auroral oval during which auroral emission is seen. As discussed above, the effective FOV for precession averaged data is ~10° in latitude which is on the scale of the latitudinal extent of the auroral oval. Thus, a second average was performed over the 50 spectra to produce a single spectrum for an entire oval crossing. This spectrum contains almost as much information as the set of 50 spectra given the extensive overlap from one spectrum to another within this set. Oval averaged spectra will be presented in the next section.

4. RESULTS

4.1 Averaged data versus time

Following the averaging of the data described in section 2.3.1, a data survey was conducted by selecting an emission feature and plotting its averaged data versus time. OI 98.9 nm was selected since it is one of the brightest features in terms of auroral emission within the observed wavelength range. The purpose of the survey was to determine times during which data were recorded for active aurora. Figures 3 through 7 show time plots of OI 98.9 nm which include dayglow and aurora (nightside and dayside). Figures 3 - 7 do not cover all of the times for which data were received from NRL. We include only times for which the auroral oval was bright enough to be seen against the underlying background. The designators N and S identify the auroral oval in the northern and southern hemispheres, respectively. SAA designates the location of the south Atlantic anomaly which contaminates the data due to energetic particles entering the instrument. The structure in Figure 3 labeled S,H^+ is due to proton aurora based on an observed enhancement in HI 121.6 nm above its geocoronal background. No other such enhancements were observed for the times covered by Figures 3 - 7. The time scale in each figure covers a period of 5000 s or 83 min which is ~80% of an entire orbit. The numbers below the time scale provide solar zenith angle at the satellite and satellite location in geographic and geomagnetic coordinates. Thus, one can identify regions such as the polar cap, equator, etc. by examining this information. It should be kept in mind, as previously discussed, that auroral structure like that in the lower panel of Figure 4 starting at 20400 s does not provide emission localized to the latitude scales given below the time scale.

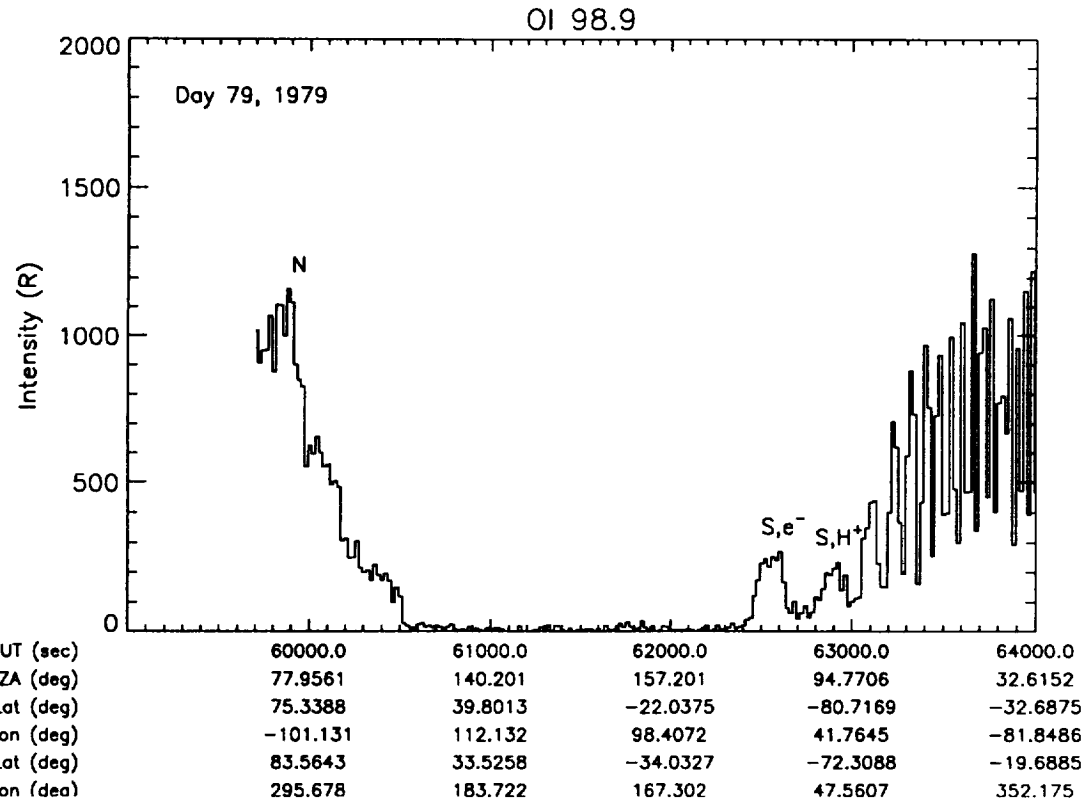

Figure 3. Nadir OI 98.9 nm versus time on Day 79, 1979 showing dayglow and auroral emission. Each data point was obtained by averaging 20 precession averaged spectra (see Figure 2 for further information concerning precession averaging). OI 98.9 nm was selected for this and the subsequent four figures because it is one of the brightest features within the wavelength range of the instrument. The values below the UT scale provide solar zenith angle at the satellite and satellite location in geographic and geomagnetic coordinates. The designator N within the figure identifies the location of the northern auroral oval on the dayside. The designators S identify the locations of the southern auroral oval on the nightside for electron and proton aurora, respectively. The proton aurora was identified from enhancements in HI 121.6 nm above the geocorona background level. Similar enhancements were not seen in the other data being addressed in this report.

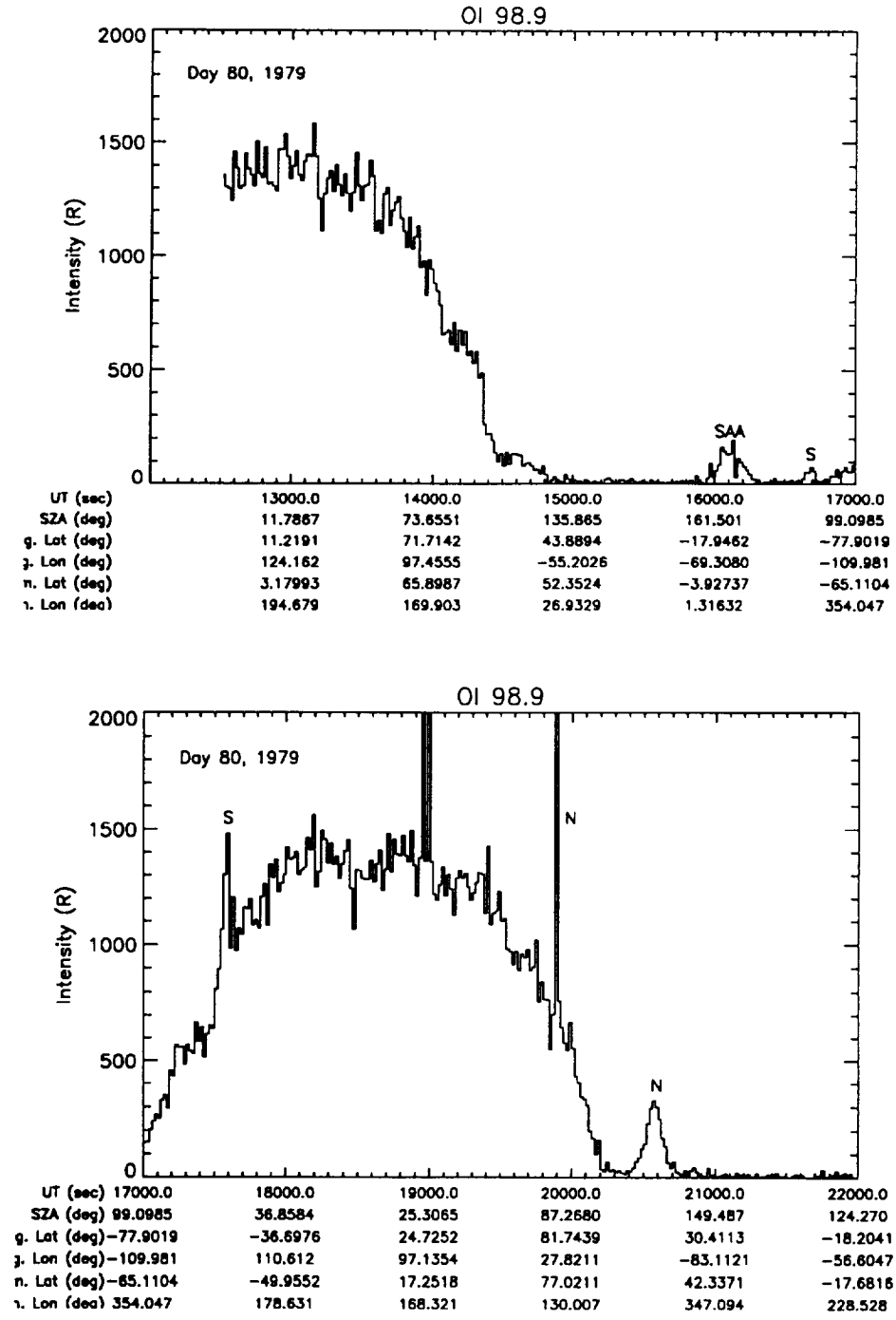

Figure 4. Similar to Figure 3 except for Day 80. The upper panel shows weak auroral emission near 16800 s with structure near 16000 s which is contaminated signal due to energetic particles entering the instrument as the satellite passed through the south Atlantic Anomaly (SAA in figure). The lower panel begins where the upper panels stops and identifies the southern auroral oval on the dayside and the northern auroral oval on the day and nightsides.

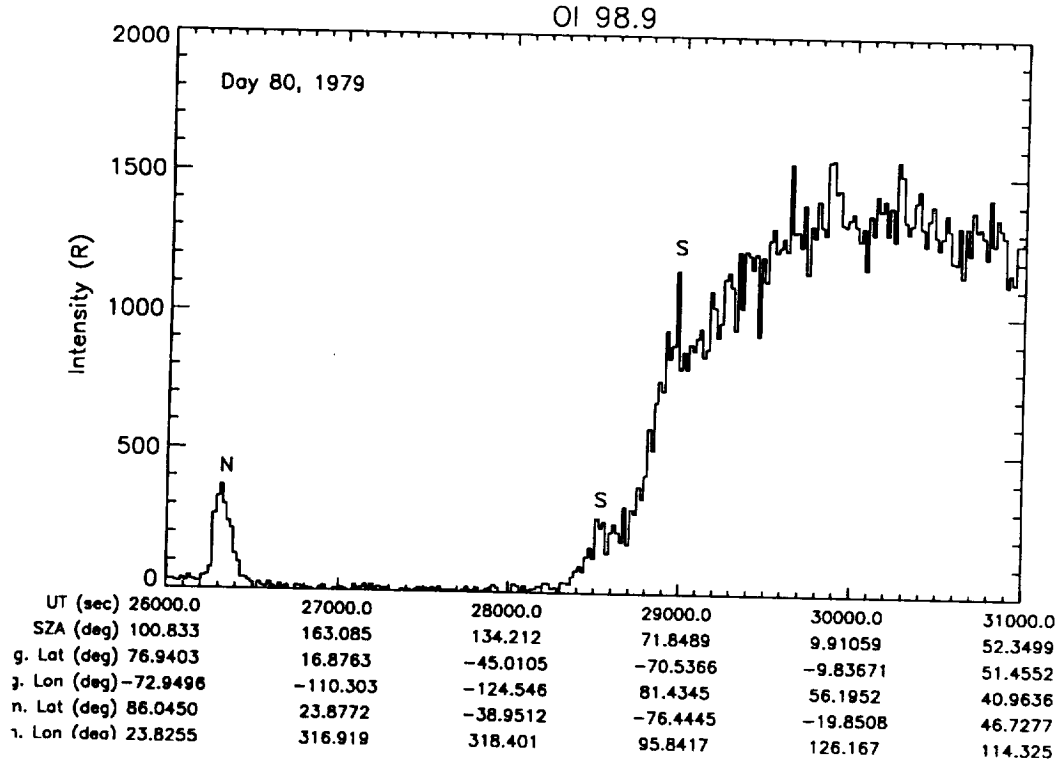

UT (sec) 26000.0	27000.0	28000.0	29000.0	30000.0	31000.0
SZA (deg) 100.833	163.085	134.212	71.8489	9.91059	52.3499
g. Lat (deg) 76.9403	16.8763	−45.0105	−70.5366	−9.83671	51.4552
g. Lon (deg) −72.9496	−110.303	−124.546	81.4345	56.1952	40.9636
n. Lat (deg) 86.0450	23.8772	−38.9512	−76.4445	−19.8508	46.7277
n. Lon (deg) 23.8255	316.919	318.401	95.8417	126.167	114.325

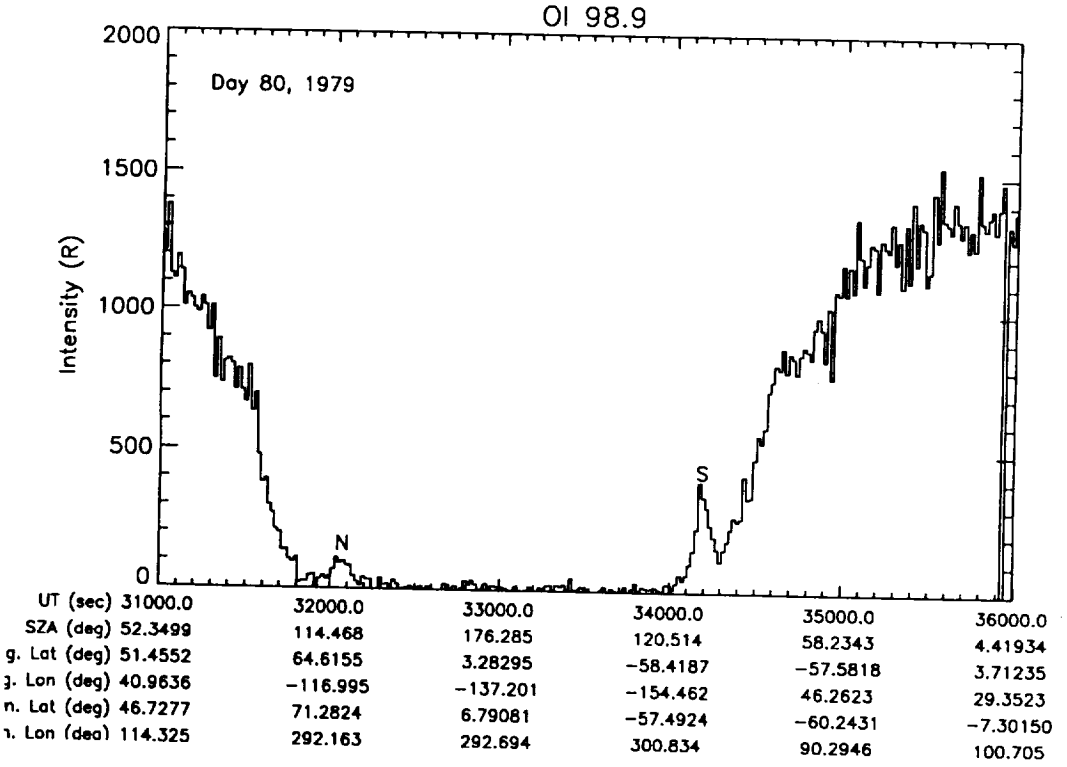

UT (sec) 31000.0	32000.0	33000.0	34000.0	35000.0	36000.0
SZA (deg) 52.3499	114.468	176.285	120.514	58.2343	4.41934
g. Lat (deg) 51.4552	64.6155	3.28295	−58.4187	−57.5818	3.71235
g. Lon (deg) 40.9636	−116.995	−137.201	−154.462	46.2623	29.3523
n. Lat (deg) 46.7277	71.2824	6.79081	−57.4924	−60.2431	−7.30150
n. Lon (deg) 114.325	292.163	292.694	300.834	90.2946	100.705

Figure 5. Similar to Figure 4 except later on Day 80.

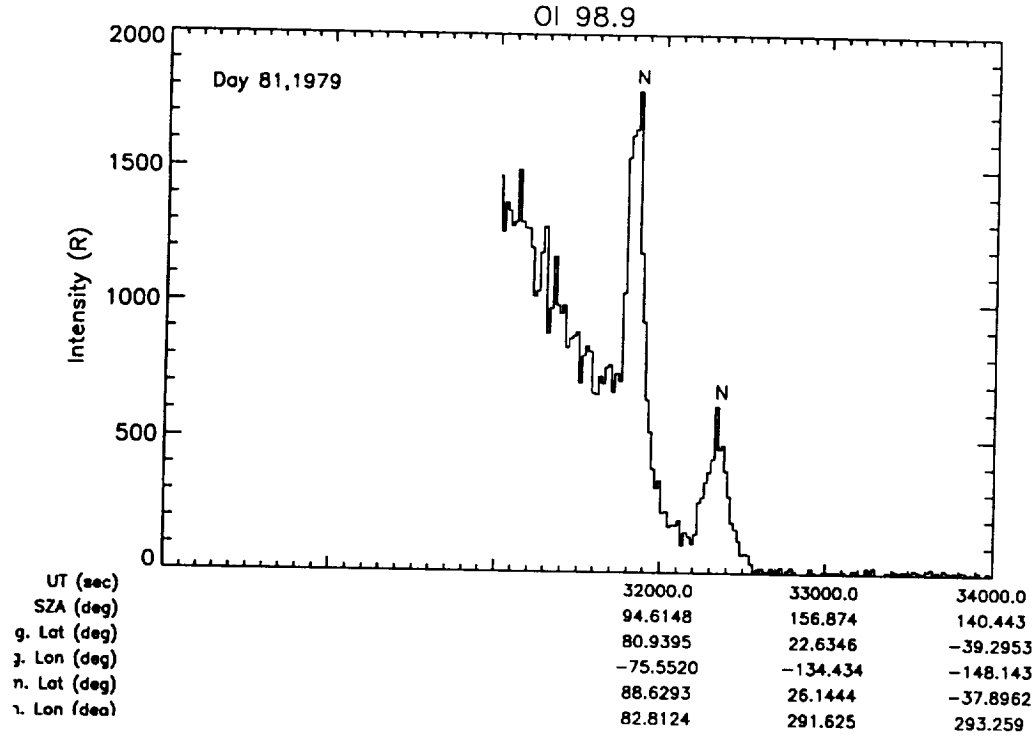

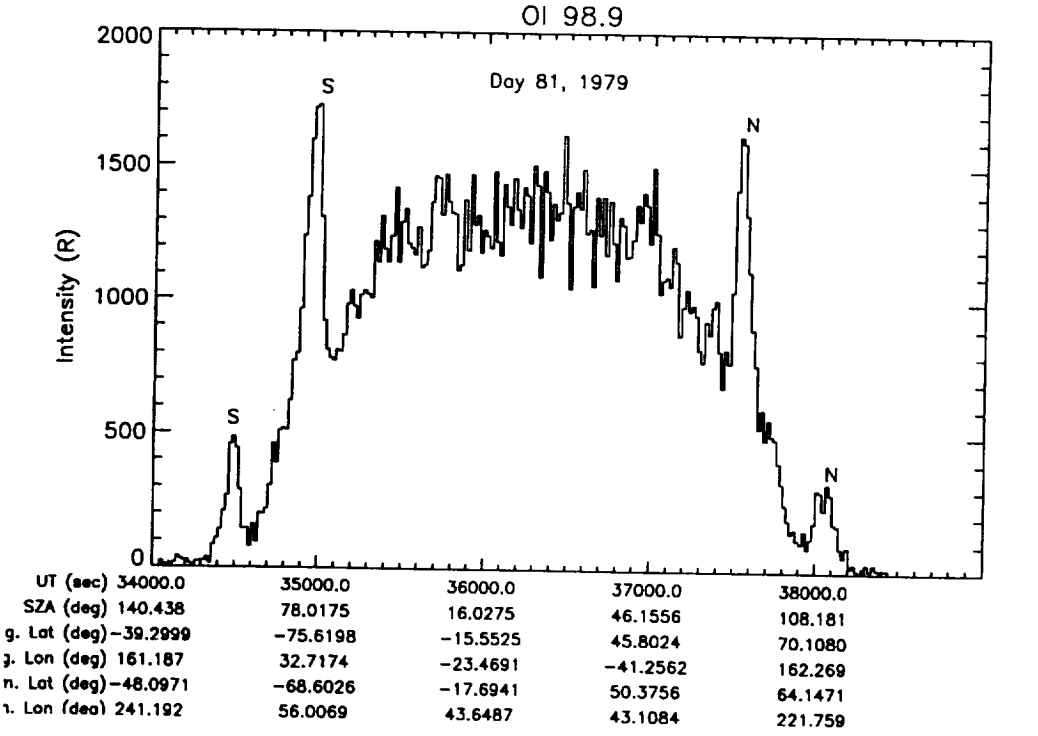

Figure 6. Similar to Figure 4 except on Day 81. Dayside and nightside aurora are prominent in these data.

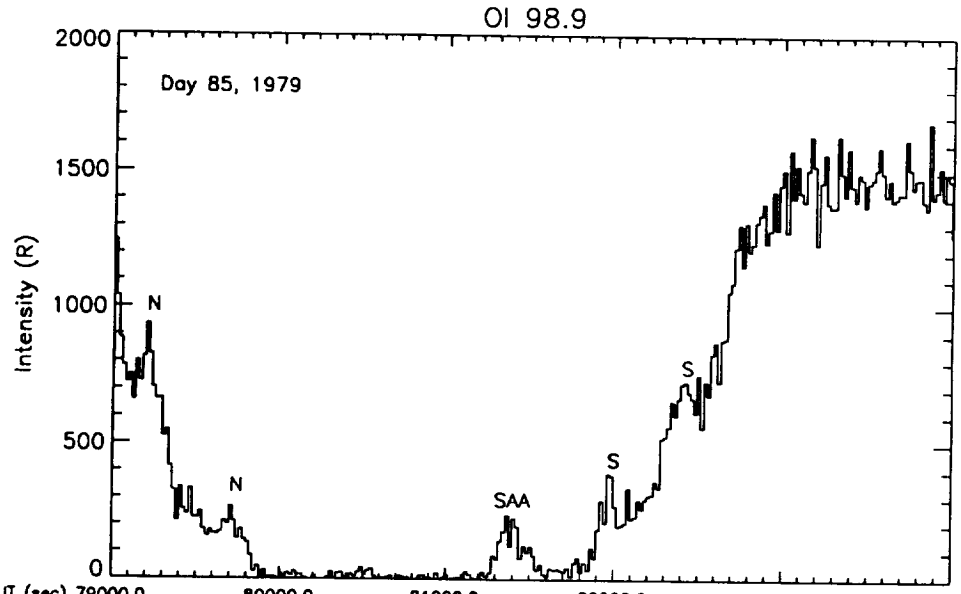

UT (sec) 79000.0	80000.0	81000.0	82000.0	83000.0	84000.0
SZA (deg) 62.5157	124.771	172.322	110.032	47.9570	13.9482
g. Lat (deg) 63.4500	52.5180	-9.36675	-70.4654	-45.3746	15.7032
g. Lon (deg)-164.990	36.5904	21.0357	-4.18015	-158.181	-172.341
n. Lat (deg) 60.3363	47.9556	-21.3193	-59.7871	-45.8951	14.5380
n. Lon (deg) 249.025	110.595	90.8209	42.2627	286.934	255.674

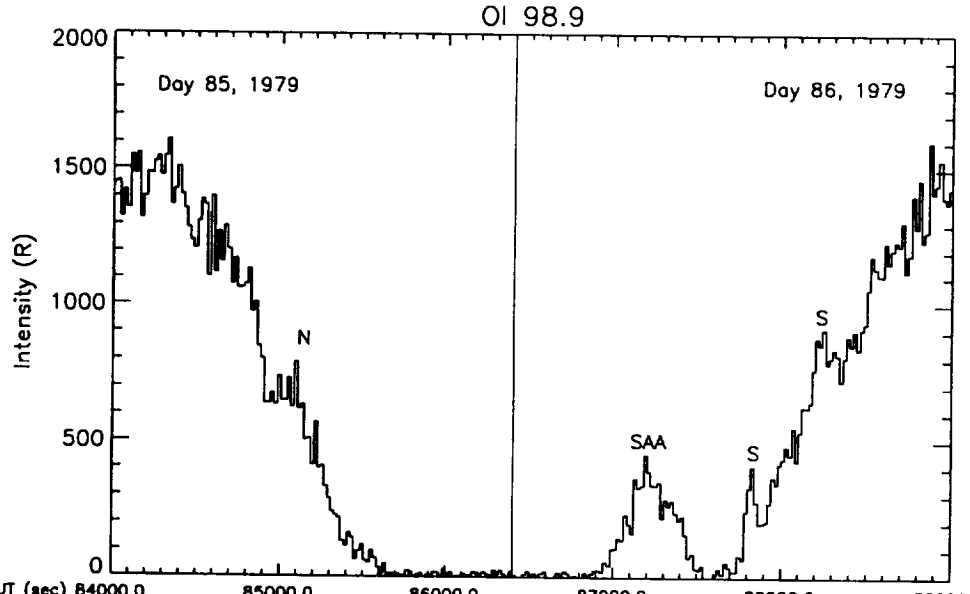

UT (sec) 84000.0	85000.0	86000.0	87000.0	88000.0	89000.0
SZA (deg) 14.2350	76.1236	138.413	158.811	96.4640	34.3236
g. Lat (deg) 15.9896	75.9090	39.0919	-22.9327	-81.1379	-31.8999
g. Lon (deg)-172.402	153.134	7.76084	-5.95495	-66.9406	173.782
n. Lat (deg) 14.7825	69.8275	32.0878	-29.0816	-65.1022	-37.7903
n. Lon (deg) 255.560	210.464	82.5716	58.4742	12.5110	252.308

Figure 7. Similar to Figure 4 except on Days 85 and 86.

4.2 Selected oval averaged spectra

Figures 8 - 11 show oval averaged spectra from selected oval crossings seen in Figures 3 - 7. The spectra in Figure 8 correspond to the electron and proton auroras in the southern hemisphere shown in Figure 3. Neither spectrum has been scaled which shows that the overall energy deposition is similar for the two events. The difference between the spectra for NII 108.5 nm is noteworthy. Much less emission is seen for the proton event. The emission is expected to be dominated by particle impact on N_2 (rather than N). In the case of proton aurora, excitation arises from H, H^+, and secondary electron impact. The spectrum of secondary electrons for proton aurora is soft (see, e.g., Basu et al., 1993 and Strickland et al., 1993) and will produce very little 108.5 nm due to the high excitation threshold (35 eV). While protons and H atoms have sufficient energy to produce 108.5 nm, the lack of emission suggests that their spectral fluxes are considerably less efficient at producing 108.5 nm than the corresponding spectral fluxes in electron aurora. Said another way, the maxima of the proton and H atom cross sections for producing 108.5 nm are smaller than that for electron impact.

Figure 9 compares the spectrum for the nightside oval crossing in the upper panel of Figure 5 with that from the lower panel. There was no enhancement of HI 121.6 nm above its background at these times which leads us to conclude that electron precipitation was responsible for the emission seen in both spectra. The OI 98.9 nm emission seen in Figure 5 for these two events is comparable. Thus, it is not surprising that the oval averaged spectra in Figure 9 are similar in magnitude. They are also seen to be similar in spectral form which is not surprising given that each is an average over the entire oval.

Figure 10 provides further comparisons among nightside oval averaged spectra. The events can be seen in the two panels of Figure 6. The differences in magnitude among the spectra are consistent with the differences in 98.9 nm seen in Figure 6. There are no pronounced differences in shape among the three spectra which again, is not surprising, given that each spectrum is an oval average.

Figure 11 compares spectra for the three dayside auroral events seen in Figure 6. The 98.9 nm feature is seen to be of about the same magnitude for the three events in both Figures 6 and 11. Differences are seen, however, in OI 102.7 nm, NII 108.5 nm, and OI 135.6 nm. There are also differences elsewhere but are not singled out due to low emission. We do not understand the cause of the differences, especially for the O emissions given that OI 98.9 nm is comparable among the three events.

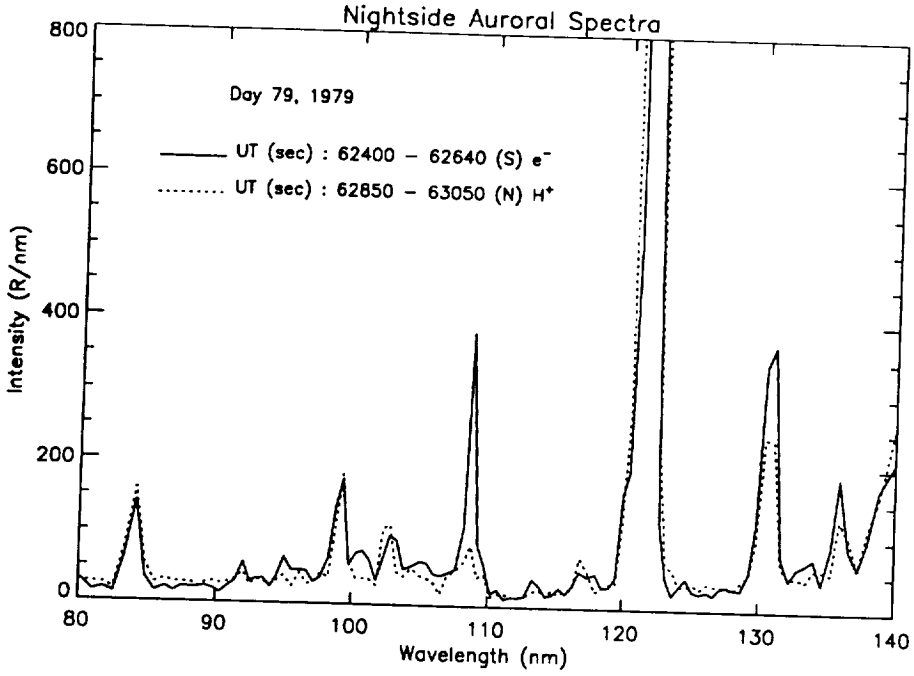

Figure 8. Average spectra for the electron and proton aurora identified in Figure 3. See Table 2 for identification of the brighter features.

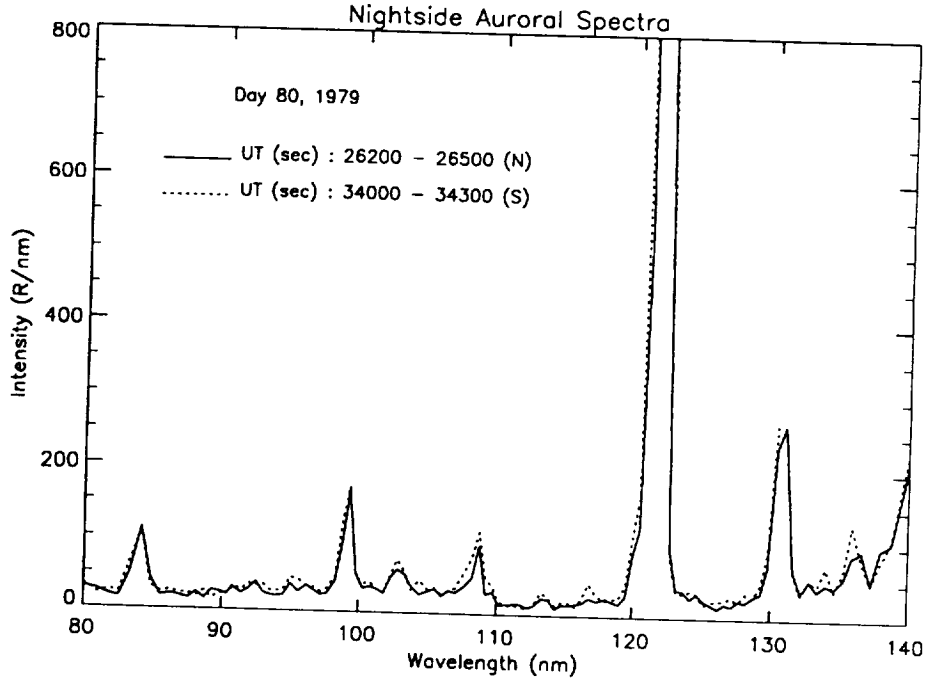

Figure 9. Average spectra for the northern auroral oval on the nightside identified in the upper panel of Figure 5 and for the southern auroral oval, also on the nightside identified in the lower panel.

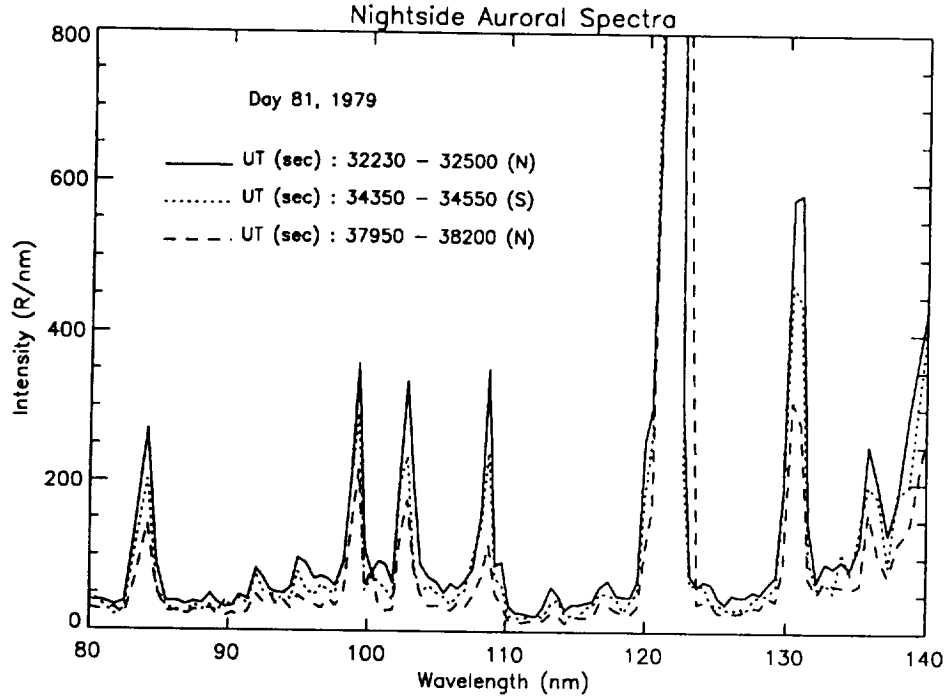

Figure 10. Average spectra for the three nightside auroras identified in Figure 6.

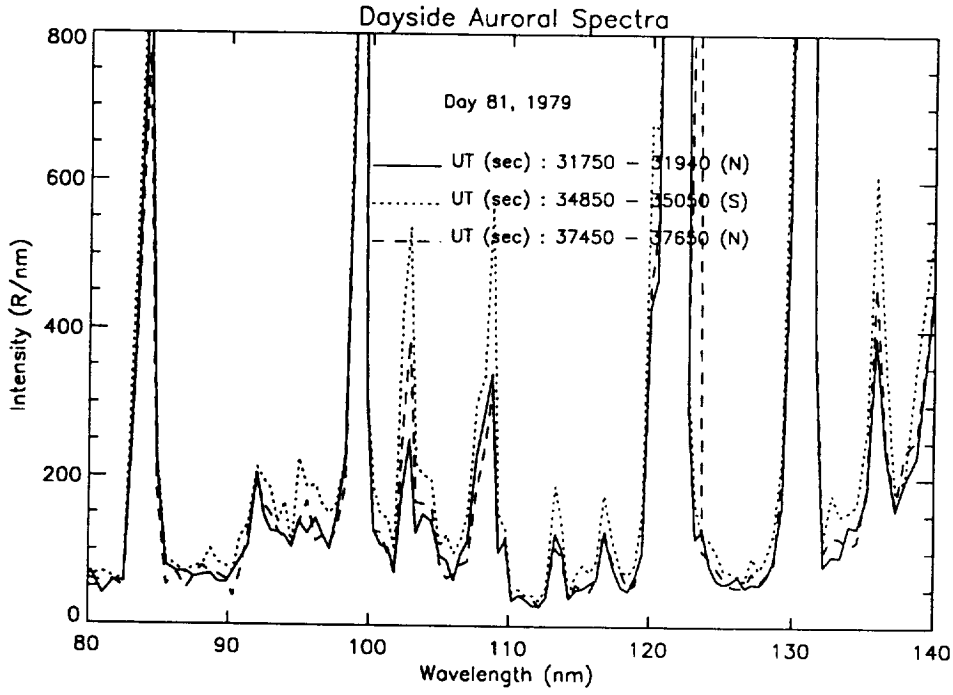

Figure 11. Average spectra for the three dayside auroras identified in Figure 6.

5. DISCUSSION AND CONCLUSIONS

We have documented an analysis performed on auroral data obtained with the U. C. Berkeley EUV/FUV instrument on-board STP 78-1. We have not performed the quantitative analysis that was originally planned under this contract. In that analysis, yield curves of key emission features versus characteristic energy of precipitating particles (electrons and protons) and versus composition were to be generated using CPI's auroral particle transport model (see, e.g., Strickland et al., 1983 and 1993). These curves were to be used to infer average spectral characteristics of particle precipitation and differences in composition within the auroral oval compared to models such as MSIS-86 (Hedin, 1987). It became apparent early in this investigation that such an analysis could not be performed due to the need to average several measurements from an experiment having a precessing line-of-sight. The averaging led to an effective FOV of ~10° in latitude for each data point. At auroral latitudes, extreme ranges in auroral conditions can be expected on this scale. Our planned quantitative analysis was then replaced by a simple examination of oval averaged spectra as discussed in section 4.2 above.

This investigation, while not producing any important insights into remote sensing of auroral regions using EUV/FUV data, is significant in pointing out a severe limitation in the Berkeley auroral data to potential users of these data. It is surprising that there has been no discussion in papers containing Berkeley auroral data on the large effective FOV that arises from the combination of a rapidly precessing look vector (4 s per precession) and low counting statistics per individual measurement. While time plots such as those presented in Figures 3 - 7 give the impression that a given data point refers to emission at some specific latitude, in reality, this is emission from a region on the width of the auroral oval from its equatorward to polarward boundaries.

6. REFERENCES

Basu, B., J. R. Jasperse, D. J. Strickland, and R. E. Daniell, Jr., Transport-Theoretic Model for the Electron-Proton-Hydrogen Atom Aurora: 1. Theory, *J. Geophys. Res.*, *98*, 21517, 1993.

Bowyer, S., R. Kimble, F. Raresce, M. Lampton, and G. Penegor, Continous readout EUV airglow spectrometer, *App. Opt.*, *20*, 477, 1981.

Chakrabarti, S., Extreme and Far Ultraviolet Emissions From the Polar Cap, *J. Geophys. Res.*, *91*, 8065, 1986.

Hedin, A.E., MSIS-86 thermospheric model, *J. Geophys. Res.*, *92*, 4649, 1987.

McPherron, R. L. and R. H. Manka, Dynamics of the 1054 UT March 22, 1979 substorm event : CDAW 6, *J. Geophys. Res.*, *90*, 1175, 1985.

Strickland, D. J., R. E. Daniell, Jr., B. Basu, and J. R. Jasperse, Transport-Theoretic Model for the Electron-Proton-Hydrogen Atom Aurora: 2. Model Results, *J. Geophys. Res.*, *98*, 21533, 1993.

Strickland, D. J., J. R. Jasperse, and J. A. Whalen, Dependence of Auroral FUV Emission on the Incident Electron Spectrum and Neutral Atmosphere, *J. Geophys. Res.*, *88*, 8051, 1983.

APPENDIX A

The O^+ 834-Å Dayglow: Revised Cross Sections

R. Link and J. S. Evans
Computational Physics, Inc.,
2750 Prosperity Avenue, Suite 600, Fairfax, VA 22031

G. R. Gladstone
Space Sciences Laboratory, University of California
Berkeley, CA 94720

Submitted to *Journal of Geophysical Research*
February 12, 1993

Abstract

This study assesses the impact of new $O(^3P)$ photoionization and N_2 photoabsorption cross sections, and O^+ oscillator strengths and transition probabilities, on OI 834-Å airglow calculations. 834-Å intensities computed using the new emission parameters are in good agreement with rocket measurements obtained in 1978 and 1980. The present study does not support a suggested reduction in the N_2 photoabsorption cross section based on an earlier analysis of the rocket data.

Introduction

The $O^+(2s^2\,2p^3\,{}^4S^\circ \leftarrow 2s\,2p^4\,{}^4P)$ 834-Å triplet is the most prominent emission below 900 Å in the terrestrial thermosphere [*Meier*, 1991]. 834-Å emission in the airglow is produced by three mechanisms, the dominant being inner shell photoionization of ground-state neutral atomic oxygen to $O^+(^4P)$. Of lesser importance is electron impact ionization of atomic oxygen which, based on the most recent cross section data, has been estimated to contribute about 5% to the peak emission intensity [*Cleary et al.*, 1989; *Meier*, 1991]. Finally, *Feldman et al.* [1981] and *Meier* [1990] estimated that resonant scattering of solar 834-Å emission provides an even smaller contribution at the peak. The 834-Å multiplet is an allowed transition, and undergoes resonant scattering by ground-state $O^+(^4S^\circ)$ ions in the ionosphere, as well as pure absorption, mainly by N_2.

In an analysis of 1978 [*Gentieu et al.*, 1979; *Feldman et al.*, 1981] and 1980 [*Gentieu et al.*, 1981, 1984] rocket observations of the 834-Å dayglow, *Cleary et al.* [1989] concluded that the observed emission intensity below about 200 km could not be explained without substantially reducing the N_2 photoabsorption cross section from the then-accepted values. Another possibility, that production of low-altitude 834-Å emission due to soft X-rays was underestimated using the solar spectrum adopted

in the model calculations, was considered unlikely due to the agreement obtained by *Link et al.* [1988*b*] and *Morrison and Meier* [1988] in their analyses of photoelectron-excited O and N_2 FUV emissions measured on the same rockets.

Meier [1991] has recently reviewed the available theoretical, laboratory and aeronomic evidence concerning the production and loss of 834-Å emission in the thermosphere; the reader is referred to that work for a synopsis of the literature. The present study assesses the impact of newer photoionization [*Bell and Stafford*, 1992] and photoabsorption [*Morgan et al.*, 1993] cross sections, and O^+ oscillator strengths and transition coefficients (K. L. Bell, *private communication*, 1992) on calculated 834-Å emission intensities.

Photoionization and Photoabsorption

Branching ratios for photoionization of $O(2s^2\,2p^3\,{}^3P)$ to the $2s\,2p^4$ states of O^+ currently used in aeronomy date back to Hartree-Fock calculations of the partial cross sections for O^+ valence shell $2s^2\,2p^3$ ($^4S^o$, $^2D^o$, $^2P^o$) and inner shell $2s\,2p^4$ (^4P, ^2P) ionization states by *Dalgarno et al.* [1964]. Using close-coupling wavefunctions, *Henry* [1967] improved the valence shell results and, after correcting an error in the statistical weights, used the inner shell $O^+(2s\,2p^4)$ cross sections of *Dalgarno et al.* [1964]

to estimate the total photoionization cross section of $O(^3P)$. Subsequently, in a comprehensive compilation of cross sections for use in aeronomy, *Kirby et al.* [1979] renormalized the partial cross sections of *Henry* [1967] to the *R*-matrix calculation of the total photoionization cross section by *Taylor and Burke* [1976].

Link et al. [1988*a*] pointed out that measurements of the total O^+ photoionization cross section by *Samson and Pareek* [1985] were significantly smaller than the values tabulated by *Kirby et al.* [1979] below 300 Å, and renormalized the tabulated partial cross sections to the experimental data. A similar procedure was adopted in an updated compilation by *Conway* [1988]. In more detailed measurements, *Angel and Samson* [1988] extended the wavelength range of the measurements of *Samson and Pareek* [1985], normalizing their new relative cross section to the latter measurements at 584 Å. Partial cross sections renormalized to the *Angel and Samson* [1988] measurements appear in a recent compilation by *Fennelly and Torr* [1992].

The essential point here is that the branching ratios for inner shell photoionization to the $2s\,2p^4$ states of O^+ appearing in the compilations by *Kirby et al.* [1979], *Conway* [1988], and *Fennelly and Torr* [1992] can be traced back to *Dalgarno et al.* [1964]. Recently, *Bell and Stafford* [1992] have calculated new cross sections for photoionization of atomic oxygen to the O^+ $2s^2\,2p^3$ ($^4S^o$, $^2D^o$, $^2P^o$) and $2s\,2p^4$ (^4P, ^2P) states using the *R*-matrix programs of *Berrington et al.* [1987]. Their calculated to-

tal photoionization cross section is in good overall agreement with the experimental data (Figure 1), although *Bell et al.* [1989] and *Bell and Stafford* [1992] note some unresolved issues which do not affect the conclusions presented herein. Also shown in Figure 1 is the *Bell and Stafford* [1992] partial cross section for photoionization to the $O^+(^4P)$ upper state of the 834-Å transition, for which no measurements are available.

Figure 2 shows the ratio of the new *Bell and Stafford* [1992] $O^+(^4P)$ cross section to the older results of *Conway* [1988] and *Fennelly and Torr* [1992]. The new results are slightly smaller at wavelengths longwards of 300 Å, where resonance structure in the theoretical calculations is evident. However, the *Bell and Stafford* [1992] branching ratios for inner shell ionization to the $2s\,2p^4$ states increase with increasing photon energy, whereas the older branching ratios are essentially constant below 300 Å. The partial cross section for photoionization to $O^+(^4P)$ is significantly larger at wavelengths below 250 Å than has been assumed, the aeronomic consequences of which are explored in this study.

The *Conway* [1988] and *Fennelly and Torr* [1992] O^+ partial cross sections are virtually identical, since the same branching ratios were adopted, and since the experimental data used to normalize the latter [*Angel and Samson*, 1988] were in turn normalized to those used in the former [*Samson and Pareek*, 1985]. The broad struc-

ture between 120 – 200 Å in Figure 2 results from scatter in the experimental data used in the respective normalizations and also from slight systematic differences between the calculated and measured cross sections (Figure 1). At wavelengths below 120 Å, the oscillations in the *Fennelly and Torr* [1992] results are a computational artifact.

In addition to new calculations of the $O(^3P)$ photoionization cross sections, K. L. Bell (*private communication*, 1992) has recently recalculated oscillator strengths and transition probabilities (Table 1) for O^+ using the CIV3 configuration interaction model [*Hibbert*, 1975], updating the results presented by *Bell et al.* [1991] where further details may be found. The newly calculated mean $O^+(^4P)$ lifetime $1.25 \times 10^{-9} s$ and total oscillator strength 0.275, with an expected accuracy of better than $\pm 10\%$ [*Bell et al.*, 1991], compare very favorably with the values of $(1.26 \pm 0.10) \times 10^{-9}\ s$ and 0.25 ± 0.03 measured by *Smith et al.* [1971]. The values tabulated by *Meier* [1991], attributed to *Ho and Henry* [1983], are actually based on the *Smith et al.* [1971] experimental oscillator strength divided amongst the multiplet components according to the statistical weights. *Ho and Henry* [1983] used CIV3 to calculate a total oscillator strength of 0.233 using a smaller number of configuration interactions.

Morgan et al. [1993] have recently measured the photoabsorption cross section of

N_2 near 834 Å at high (0.008-Å) resolution. Shown in Figure 3 and listed in Table 1 are their measurements using an O^+ emission source (triangles) at the positions of the $O^+(^4P)$ triplet lines. The measurements were repeated over a broader wavelength range (solid lines) using a synchrotron source, in order to resolve the N_2 rotational structure. As can be seen from Figure 3, only the $^4P_{3/2}$ 834.47-Å component undergoes significant absorption by N_2. While the new photoabsorption cross section for this line (1/2 total weight) is in reasonable agreement with the low-resolution results listed in the most recent tabulation by *Fennelly and Torr* [1992], the cross sections for the 833.33 and 832.76-Å components (Table 1) are smaller by one and two orders of magnitude respectively.

To our knowledge, there are no recent high-resolution measurements of the photoabsorption cross section of O_2 near 834 Å. The measurements of Hudson and Carter reported by *Hudson* [1971] are shown in Figure 4. Also indicated in that figure are the positions of the 834-Å triplet lines. *Hudson* [1971] cautions that use of the *Matsunaga and Watanabe* [1967] O_2 photoabsorption cross section (dashed line), recommended by *Fennelly and Torr* [1992], will lead to a wrong attenuation profile for the 833.33-Å component of the $O^+(^4P)$ emission. However, as this line accounts for only 1/3 of the total weight, the effect on the multiplet intensity is not large.

It is important to note here that for the 834.47-Å line, only absorption by N_2 is important, while for the 833.33 and 832.76-Å components, only absorption by O_2 is significant, based on the present photoabsorption cross sections. A new measurement of the O_2 photoabsorption cross section at higher resolution is warranted. Also, it should be noted that the laboratory measurements were performed at 300 K while in the 100 – 200 km altitude region where absorption of 834-Å emission is important, the thermospheric temperature increases from 200 K to about 1000 K, depending upon solar activity. Nevertheless, the measurements at 300 K provide reasonable fits to the observations presented below, as most of the absorption occurs at the bottom of this altitude region where the absorber densities are greatest and temperatures are near 300 K.

Model Description

In the following sections, we assess the implications of the new atomic and molecular parameters for the O^+ 834-Å dayglow. Excitation rates computed using the old and new photoionization cross sections are compared. Our model results then are compared to rocket measurements of 834-Å dayglow intensity profiles, and to a previous analysis of the rocket data which inferred problems with the N_2 photoabsorption cross

section. The sensitivity of these results to the O^+ density profile is examined. We then briefly discuss implications for extraction of O^+ densities from satellite measurements of the 834-Å emission. Here, we summarize changes to our models since the analysis by *Link et al.* [1988*b*] of OI and N_2 emissions measured on the same rocket flights.

Photoionization and photoelectron production rates are computed [*Link*, 1992, Appendix B] using the same solar EUV spectra adopted by *Link et al.* [1988*b*]. The new calculations use the N_2 and O_2 photoabsorption and total photoionization cross sections tabulated by *Conway* [1988]. These cross sections do not differ appreciably from those of *Fennelly and Torr* [1992] except for N_2 photoabsorption at wavelengths longer than about 730 Å, where the latter authors have performed a higher-resolution discretization of the laboratory data. We have adopted the *Fennelly and Torr* [1992] N_2 values for wavelengths longer than the first ionization threshold (796 Å). Partial photoionization cross sections for N_2 and O_2 are taken from *Conway* [1988]. The cross sections of *Bell and Stafford* [1992] have been adopted for atomic oxygen.

The present calculations of the 834-Å intensity include the contribution from photoelectron impact, which is calculated using the 2-stream Feautrier transport model of *Link* [1992] for energies up to 355 eV. The *Zipf et al.* [1985] cross section for electron impact ionization of $O(^3P)$ to $O^+(^4P)$ is used here. The angle-averaged,

non-isothermal, partial frequency redistribution radiative transfer model of *Gladstone* [1988] described by *Link et al.* [1988*a*] is used to calculate resonance scattering and pure absorption of 834-Å photons originating from photoionization, photoelectron impact, and scattering of solar 834-Å radiation. The latter is calculated by apportioning 26% of the solar 834-Å irradiance, a blend of OI and OII lines, to O^+ [*Meier et al.*, 1990]. Parameters appearing in the radiative transfer calculation are summarized in Table 1. These are: the line center wavelength [*Eriksson*, 1987], cross sections for photoabsorption by N_2 [*Morgan et al.*, 1993], O_2 [*Hudson*, 1971] and O [*Bell and Stafford*, 1992], OI oscillator strengths and transition coefficients (K. L. Bell, *private communication*, 1992), scattering cross sections (calculated from the new oscillator strengths) and Voigt parameters at a reference temperature of 1000 K, and the Rayleigh fraction of the scattering phase function [*Chandrasekhar*, 1960, p. 52].

We have compared the results using our new models and cross sections to the calculations published by *Link et al.* [1988*b*]. The only notable (but minor) difference in computed OI and N_2 intensities arises from our use of MSIS-86 [*Hedin*, 1987], instead of MSIS-83 [*Hedin*, 1983], in specifying the thermospheric composition and temperature. Photoelectron fluxes calculated using the old and new photoabsorption and photoionization cross sections are experimentally indistinguishable. We have also compared the isothermal, complete frequency redistribution approximation employed

in previous analyses of the 834-Å dayglow to the non-isothermal, partial frequency redistribution results, both calculated using the model of *Gladstone* [1988]. Due to the low number of scatterings (line-center triplet optical depths of the order of 5 – 10), there is no significant difference in 834-Å intensities between these approximations.

Comparison with the Rocket Data

In this section, we assess the impact of the new cross sections and oscillator strengths on calculations of the 834-Å dayglow emission. Model results are compared to 834-Å dayglow intensities measured by two rocket experiments in 1978 [*Gentieu et al.*, 1979; *Feldman et al.*, 1981] and 1980 [*Gentieu et al.*, 1981, 1984]. Launch conditions and EUV spectrometer characteristics are given in Table 2, where errors in longitude and in the $F_{10.7}$ solar activity index appearing in some previous analyses of these data are corrected. Comparisons are presented here with the rocket measurements at 90° zenith viewing angle. *Link et al.* [1988*b*] previously reported an analysis of OI and N_2 EUV – FUV emissions measured on these flights, and further details of the experiments and model computations may be found therein.

Shown in Figure 5a are production rates calculated for the conditions of the 1978 launch. The dotted curve shows the production of 834-Å emission by photoionization,

calculated using the $O^+(^4P)$ cross section of *Link et al.* [1988*a*] (see previous section) which is essentially the same as that of *Conway* [1988] and *Fennelly and Torr* [1992]. The dashed curve shows the result using the new *Bell and Stafford* [1992] photoionization cross section. As mentioned previously (see Figure 2), the new cross section is slightly smaller at wavelengths longwards of 300 Å, resulting in a slight decrease in 834-Å production in the F region. However, solar soft X-rays become relatively more important with the increase in the cross section at shorter wavelengths, resulting in a substantial increase in the 834-Å production rate at E-region altitudes. This increase is compounded when the photoelectron contribution is added (solid line). Interestingly, adding photoelectrons almost exactly compensates for the slight decrease in the F region, yielding a total production rate above 175 km almost identical to that obtained using the old photoionization cross section and neglecting photoelectrons (dotted curve).

In Figure 5b, intensities calculated for 90° viewing angle using the old photoionization cross section are compared to those computed using the new cross section together with the additional photoelectron and solar resonance scattering sources. As may be seen, the dramatic increase in the E-region 834-Å production rate (Figure 5a) is mitigated by absorption by N_2 and O_2. Figure 5c shows the contributions of photoionization, photoelectron impact, and resonance scattering of solar OII 834-

Å emission to the total multiplet intensity shown in Figure 5b (solid curve). As can be seen, the photoelectron and solar line sources are not negligible above the emission peak, contributing about 20 – 25% when viewing horizontally at altitudes 300 – 400 km.

Figure 6a shows a comparison of our model results to the 1978 rocket measurements. Calculations were performed for two different model O^+ profiles (Figure 6b) obtained using the IRI-90 [*Bilitza*, 1990] and ICED [*Tascione et al.*, 1988] empirical ionospheric models. These profiles were normalized to the peak electron density (1.36×10^6 cm^3 at 281 km) measured by an ionosonde at White Sands at the time of launch. We have assumed the O^+ and electron densities to be equal. Although this assumption is not valid in the E and F_1 regions, photoabsorption of 834-Å photons by N_2 and O_2 dominates resonance scattering by O^+ at these altitudes, as can be seen in the similarity between the two computed intensity profiles. Given the uncertainty in the topside plasma density, we consider the agreement with the rocket measurements to be acceptable.

Figures 7a,b show corresponding results for the 1980 rocket. As no ionosonde measurements are available for White Sands on that date, ICED and IRI-90 densities were used. The O^+ density profile computed by *Cleary et al.* [1989] in their analysis

of these same data yielded a peak density and altitude in good agreement with the IRI-90 result shown in Figure 7b. However, ionosonde measurements at Boulder gave a peak electron density of 5.90×10^5 cm^3 at 485 km, considerably different from the computed profiles. Nevertheless, we obtain a reasonable fit to the 834-Å measurements (Figure 7a). The model results appear to be in slightly better agreement with the downleg data than with the upleg above 200 km. We slightly overestimate the observed intensity, as was the case for the photoelectron-excited OI 1356-Å and N_2 LBH emissions reported by *Link et al.* [1988*b*]. A small reduction in the model solar EUV irradiance would ameliorate this simultaneous overestimate of the OI, OII, and N_2 intensities.

Comparison with Previous Calculations

The 1978 rocket measurements discussed in the preceding section were first analyzed by *Feldman et al.* [1981]. The model calculations were later revised by *Cleary et al.* [1989], who also examined the 1980 data. Normalizing their computed intensities to match the rocket data above 200 km, *Cleary et al.* [1989] found that the shape of their profiles did not agree with the observations, with the model underestimating the observed intensities at lower altitudes. In order to remedy this situation, *Cleary et al.*

[1989] postulated a decrease by an order of magnitude in the photoabsorption cross section of N_2 reported by *Hudson and Carter* [1969]. Another possibility, an increase in the solar EUV flux below 200 Å, was discounted due to the agreement obtained by *Morrison and Meier* [1988] and by *Link et al.* [1988*b*] with OI and N_2 EUV – FUV airglow measured on the same rockets. Here, we have obtained agreement with the rocket 834-Å measurements without requiring a reduction in the N_2 photoabsorption cross section.

We briefly discuss the differences between the present results and those of *Cleary et al.* [1989]. For photoionization of atomic oxygen, *Cleary et al.* [1989] used the total cross section of *Samson and Pareek* [1985] and the branching ratios of *Henry* [1967]. A total oscillator strength of 0.43 *Wiese et al.* [1966] was adopted. The difference in the adopted oscillator strengths does not appreciably affect the intensities for the rocket viewing geometry. The isothermal, complete frequency redistribution code described by *Strickland and Anderson* [1983] and *Anderson and Meier* [1985] was used to calculate multiple scattering of 834-Å photons by *Cleary et al.* [1989].

We both used the *Hinteregger et al.* [1981] model to specify the solar EUV irradiance although in the present case, we [*Link et al.*, 1988*b*] supplanted the model values with AE-E satellite measurements obtained from the SC#21OBS [*Hinteregger et al.*, 1981] daily summary of selected wavelength groups. *Cleary et al.* [1989] scaled the

model solar irradiances by factors of 1.3 (1978) and 0.9 (1980), for consistency with *Morrison and Meier* [1988]. We have used MSIS-86 [*Hedin*, 1987] to specify thermospheric composition, while *Cleary et al.* [1989] used MSIS-83 [*Hedin*, 1983] with the model atomic oxygen abundance scaled by a factor of 0.7 in the 1980 case, again for consistency with *Morrison and Meier* [1988]. Intensities computed by *Cleary et al.* [1989] for the 1980 case were scaled upwards by a factor of 1.15 in order to match the observations above 200 km. The normalization factor for the 1978 case was not stated.

We do not fully understand the differences in the shape of the 834-Å emission intensity profiles determined by *Cleary et al.* [1989] and those presented here. *Cleary et al.* [1989] underestimated the emission intensities below 200 km, which they suggested may be due to problems with the N_2 photoabsorption cross section. The recent measurements of *Morgan et al.* [1993] show that this is not the case. As can be seen from Figure 5b, using the new photoionization cross section [*Bell and Stafford*, 1992] and including the photoelectron contribution does not resolve this problem, since absorption masks the differences in the computed excitation rate profiles. Another possibility is the following. An error has been found (R. R. Meier, *private communication*, 1990) in the statistical weights of the 832 and 833-Å lines in the code (D. J. Strickland, unpublished) used by *Cleary et al.* [1989] to calculate the total triplet

excitation rate such that these are 1/2 of the correct weights. As these components undergo relatively little absorption by N_2 compared to the 834-Å line, the shape of the low-altitude profiles will be distorted, and the overall intensities will be underestimated.

In the 1978 case, we fit the 834-Å data (Figure 6a) using the *Hinteregger et al.* [1981] solar flux. However, *Link et al.* [1988*b*] and *Morrison and Meier* [1988] required increases by factors of 1.5 and 1.3 respectively in the photoelectron production rate in order to fit the OI and N_2 LBH intensities measured on the same rocket. The reasons for this discrepancy between the 1978 834-Å and the photoelectron-excited OI and N_2 emissions is not clear. No substantial adjustment to the solar EUV or photoelectron production rate is required to fit the 1980 834-Å or OI and N_2 emissions. Although the EUV 834-Å and the FUV OI and N_2 emissions were measured by different spectrometers, we do not believe this to be a problem since within the region of wavelength overlap, the observed HI Ly_α intensities agreed to within 4% [*Gentieu et al.*, 1979]. The difference between the *Link et al.* [1988*b*] and the *Morrison and Meier* [1988] solar EUV adjustment is due to differences in the adopted OI 1356-Å excitation cross sections, in the adopted solar EUV spectra, and in the adopted atomic oxygen abundances. A detailed examination of the models and cross sections used in these studies is now in progress, and the results will be reported in a future

publication.

Conclusions

The 834-Å dayglow now appears to be well-understood. The photoionization cross sections of *Bell and Stafford* [1992], the N_2 photoabsorption cross sections of *Morgan et al.* [1992], and the O^+ oscillator strengths and transition probabilities of Bell (*private communication*, 1992) produce agreement with the 1978 and 1980 834-Å rocket airglow measurements. The revised photoionization and photoabsorption cross sections and neglect of photoelectrons have no significant impact on remote sensing of ionospheric plasma densities by satellite. The lower oscillator strengths indicate that the 834-Å emission undergoes less scattering by ionospheric (or magnetospheric) $O^+(^4S^\circ)$ ions than originally estimated.

Acknowledgements

We greatly appreciate the efforts of K. L. Bell in providing us with new calculations of the photoionization cross sections for atomic oxygen, and for providing new O^+ oscillator strengths and transition probabilities ahead of publication. We are indebted

to H. Morgan for providing us with his N_2 photoabsorption measurements prior to publication. We thank R. R. Conway and J. Fennelly for providing us with their cross section compilations. We also thank D. D. Cleary, R. R. Meier, and D. J. Strickland for helpful discussions. This work was supported by NASA awards NASW-4744 (RL and JSE) and NAG5-1507 (GRG).

References

Anderson, D. E., Jr., and R. R. Meier, The OII 834-Å dayglow: A general model for excitation rate and intensity calculations, *Planet. Space Sci.*, *33*, 1179, 1985.

Angel, G. C., and J. A. R. Samson, Total photoionization cross sections of atomic oxygen from threshold to 44.3 Å, *Phys. Rev.* A, *38*, 5578, 1988.

Bell, K. L., and R. P. Stafford, Photoionization cross sections for atomic oxygen, *Planet. Space Sci.*, *40*, 1419, 1992.

Bell, K. L., P. G. Burke, A. Hibbert, and A. E. Kingston, Photoionization of the $2p^4\,{}^3P$, ${}^1D$ and ${}^1S$ states of atomic oxygen, *J. Phys. B: At. Mol. Phys.*, *22*, 3197, 1989.

Bell, K. L., A. Hibbert, B. M. McLaughlin, and K. Higgins, Oscillator strengths for optically allowed transitions from the $2s^2\,2p^3\,{}^4S^\circ$, ${}^2D^\circ$ and ${}^2P^\circ$ states of singly ionized oxygen, *J. Phys. B: At. Mol. Phys.*, *24*, 2665, 1991.

Berrington, K. A., P. G. Burke, K. Butler, M. J. Seaton, P. Storey, K. T. Taylor, and Yu Yan, Atomic data for opacity calculations: II. Computational methods, *J. Phys. B: At. Mol. Phys.*, *20*, 6379, 1987.

Bilitza, D., International Reference Ionosphere 1990, National Space Science Data Center, *NSSDCA/WDC-A-R&S 90-20*, Greenbelt, MD, 1990.

Chandrasekhar, S., *Radiative Transfer*, Dover, New York, 1960.

Cleary, D. D., R. R. Meier, E. P. Gentieu, P. D. Feldman, and A. B. Christensen, An analysis of the effects of N_2 absorption on the O^+ 834-Å emission from rocket observations, *J. Geophys. Res.*, *94*, 17,281, 1989.

Conway, R. R., Photoabsorption and photoionization cross sections of O, O_2, and N_2 for photoelectron calculations: A compilation of recent measurements, Naval Research Laboratory, *NRL Memo. Rep. 6155*, Washington, 1988.

Dalgarno, A., R. J. W. Henry, and A. L. Stewart, The photoionization of atomic oxygen, *Planet. Space Sci.*, *12*, 235, 1964.

Eriksson, K. B. S., Accurate wavelengths in OII, *J. Opt. Soc. Am.*, *4*, 1369, 1987.

Feldman, P. D., D. E. Anderson, Jr., R. R. Meier, and E. P. Gentieu, The ultraviolet dayglow 4. The spectrum and excitation of singly ionized oxygen, *J. Geophys. Res.*, *86*, 3583, 1981.

Fennelly, J. A., and D. G. Torr, Photoionization and photoabsorption cross sections of O, N_2, O_2, and N for aeronomic calculations, *At. Data Nucl. Data Tables*, *51*, 231, 1992.

Gentieu, E. P., P. D. Feldman, and R. R. Meier, Spectroscopy of the extreme ultraviolet dayglow at 6.5-Å resolution: Atomic and ionic emissions between 530 and 1240 Å, *Geophys. Res. Lett.*, *6*, 325, 1979.

Gentieu, E. P., P. D. Feldman, R. W. Eastes, and A. B. Christensen, Spectroscopy of

the extreme ultraviolet dayglow during active solar conditions, *Geophys. Res. Lett.*, *8*, 1242, 1981.

Gentieu, E. P., P. D. Feldman, R. W. Eastes, and A. B. Christensen, EUV airglow during active solar conditions 2. Emission between 530 and 930 Å, *J. Geophys. Res.*, *89*, 11,053, 1984.

Gladstone, G. R., UV resonance line dayglow emissions on Earth and Jupiter, *J. Geophys. Res.*, *93*, 14,623, 1988.

Hedin, A. E., A revised thermospheric model based on mass spectrometer and incoherent scatter data: MSIS-83, *J. Geophys. Res.*, *88*, 10,170, 1983.

Hedin, A. E., MSIS-86 thermospheric model, *J. Geophys. Res.*, *92*, 4649, 1987.

Henry, R. J. W., Photoionization cross sections for atomic oxygen, *Planet. Space Sci.*, *15*, 1747, 1967.

Hibbert, A., A general program to calculate configuration interaction wave functions: electric oscillator dipole strengths, *Comput. Phys. Comm.*, *9*, 141, 1975.

Hinteregger, H. E., K. Fukui, and B. R. Gibson, Observational reference and model data on solar EUV, from measurements on AE-E, *Geophys. Res. Lett.*, *8*, 1147, 1981.

Ho, Y. K., and R. J. W. Henry, Oscillator strengths and collision strengths for OI and OII, *Astrophys. J.*, *264*, 733, 1983.

Hudson, R. D., Critical review of ultraviolet photoabsorption cross sections for molecules

of astrophysical and aeronomic interest, *Rev. Geophys.*, *9*, 305, 1971.

Hudson, R. D., and V. L. Carter, Predissociation in N_2 and O_2, *Can. J. Chem.*, *47*, 1940, 1969.

Kirby, K., E. R. Constantinides, S. Babeu, M. Oppenheimer, and G. A. Victor, Photoionization and photoabsorption cross sections of He, O, N_2 and O_2 for aeronomic calculations, *At. Data Nucl. Data Tables*, *23*, 63, 1979.

Link, R., Feautrier solution of the electron transport equation, *J. Geophys. Res.*, *97*, 159, 1992.

Link, R., S. Chakrabarti, G. R. Gladstone, and J. C. McConnell, An analysis of satellite observations of the OI EUV dayglow, *J. Geophys. Res.*, *93*, 2693, 1988a.

Link, R., G. R. Gladstone, S. Chakrabarti, and J. C. McConnell, A reanalysis of rocket measurements of the ultraviolet dayglow, *J. Geophys. Res.*, *93*, 14,631, 1988b.

Matsunaga, F. M., and K. Watanabe, Total and photoionization coefficients and dissociation of O_2 in the 580 - 1070 Å region, *Sci. Light*, *16*, 31, 1967.

Meier, R. R., The scattering rate of solar 834-Å radiation by magnetospheric O^+ and O^{++}, *Geophys. Res. Lett.*, *17*, 17, 1990.

Meier, R. R., Ultraviolet spectroscopy and remote sensing of the upper atmosphere, *Space Sci. Revs.*, *58*, 1, 1991.

Meier, R. R., K. G. Widing, and U. Feldman, Analysis of the solar OI/OII multiplets at

834 Å: Implications for the emission measure distribution in the vicinity of 40,000 K, *Astrophys. J.*, *369*, 570, 1991.

Morgan, H. D., H. M. Seyoum, J. D. E. Fortna, D. C. Humm, A. Asfaw, and D. D. Cleary, Total photoabsorption cross section of molecular oxygen near 83.4 nm, *J. Geophys. Res.*,, in press, 1993.

Morrison, M. D., and R. R. Meier, The OI 989 and 1173 Å multiplets in the dayglow, *Planet. Space Sci.*, *36*, 987, 1988.

Samson, J. A. R., and P. N. Pareek, Absolute photoionization cross sections of atomic oxygen, *Phys. Rev.* A, *31*, 1470, 1985.

Smith, W. H., J. Bromander, L. J. Curtis, H. G. Berry, and R. Buchta, Lifetime measurements and absolute oscillator strengths for some vacuum-ultraviolet transitions in OI and OII, *Astrophys. J.*, *165*, 217, 1971.

Strickland, D. J., and D. E. Anderson, Jr., Radiation transport effects on the OI (1356-Å) limb intensity profile in the dayglow, *J. Geophys. Res.*, *88*, 9260, 1983.

Tascione, T. F., H. W. Kroehl, R Creiger, J. W. Freeman, Jr., R. A. Wolf, R. W. Spiro, R. V. Hilmer, J. W. Shade, and B. A. Hausman, New ionospheric and magnetospheric specification models, *Radio Sci.*, *23*, 211, 1988.

Taylor, K. T., and P. G. Burke, Photoionization of ground-state carbon and oxygen

atoms, *J. Phys. B: At. Mol. Phys.*, 9, L*353*, 1976.

Wiese, W. S., M. W. Smith, and B. M. Glennon, *Atomic transition probabilities, Vol. 1: Hydrogen through neon*, National Bureau of Standards, Gaithersburg, Md., 1966.

Zipf, E. C., W. W. Kao, and P. W. Erdman, On the simultaneous ionization-excitation of the OII(λ834 Å) resonance transition by electron impact on atomic oxygen, *Planet. Space Sci.*, *33*, 1309, 1985.

Table 1. $O^+(2s^2\,2p^3\,{}^4S^\circ \leftarrow 2s\,2p^4\,{}^4P)$ 834-Å Radiative Parameters

Upper State	Statistical Weight	Wavelength (Å)	Oscillator Strength	Transition Coefficient (s^{-1})	Scattering Cross Section 1000 K, (cm^2)	Voigt Parameter 1000 K	Rayleigh Fraction	Absorption Cross Section N_2 (Mb)	O_2 (Mb)	O (Mb)
5/2	6	834.4655	0.1371	8.757×10^8	1.68×10^{-13}	5.70×10^{-3}	0.28	10.1	10.44	3.90
3/2	4	833.3294	0.0916	8.799×10^8	1.12×10^{-13}	5.73×10^{-3}	0.32	0.29	14.40	3.89
1/2	2	832.7572	0.0459	8.821×10^8	5.61×10^{-14}	5.74×10^{-3}	0.00	0.049	31.80	3.89

Table 2. Experiment Parameters

Launch Conditions		
NASA Rocket	25.029 GA	25.046 CE
Launch Date	January 9, 1978	June 27, 1980
Local Time	1300 MST	1300 MDT
Latitude	32.4° N	
Longitude	106.3° W	
$F_{10.7}$	100.3	212.6
$F_{10.7}$ (previous day)	106.3	226.3
$\bar{F}_{10.7}$	115.9	201.4
A_p	23	3
Solar Zenith Angle	55.6°	9.3°
T_∞ (MSIS-86)	974.7 K	1385.8 K

EUV Spectrometer Characteristics		
Wavelength Range	530 – 1250 Å	
Resolution	8 Å	3.5 Å
Field of View	10° × 10°	8° × 8°
Calibration Uncertainty	±20%	±30%

List of Figures

Fig. 1 Cross section for photoionization of $O(^3P)$. The upper and lower curves are respectively the total and $O^+(^4S^\circ)$ cross sections calculated by *Bell and Stafford* [1992]. The symbols show measurements of the total cross section by *Samson et al.*

Fig. 2 Ratio of the *Bell and Stafford* [1992] $O^+(^4S^\circ)$ cross section to values tabulated by *Conway* [1988] and *Fennelly and Torr* [1992].

Fig. 3 The photoabsorption cross section of N_2 near 834 Å [*Morgan et al.*, 1993]. Triangles indicate the more accurate O^+ emission source measurements at the 834-Å triplet components; solid lines show synchrotron measurements of the N_2 rotational structure. Estimated error bars on the emission measurements are smaller than the triangles in panels (a) and (b).

Fig. 4 The photoabsorption cross section of O_2 near 834 Å measured by (solid line) Hudson and Carter [*Hudson*, 1971] and by (dashed line) *Matsunaga and Watanabe* [1967]. Also indicated are the positions of the OII 834-Å triplet lines.

Fig. 5 (a) Calculated 834-Å excitation rates: (dotted line) photoionization only, using the *Henry* [1967] branching ratios, (dashed line) photoionization only, using the *Bell and Stafford* [1992] cross section, and (solid line) adding photoelectron impact excitation and solar resonance scattering to the latter. mbox(b) Intensities computed from (a) for 90° zenith viewing angle. (c) Contributions to the total intensity.

Fig. 6 (a) Model ionosphere profiles used to calculate resonance scattering of 834-Å emission for the 1978 case. The profiles are scaled to the peak density measured by ionosonde. (b) Intensities computed for 90° zenith viewing angle, using the profiles given in (a), compared to the rocket measurements.

Fig. 7 (a) Model ionosphere profiles used to calculate resonance scattering of 834-Å emission for the 1980 case. The model profiles are not scaled. (b) Intensities computed for 90° zenith viewing angle, using the profiles given in (a), compared to the rocket measurements.

Fig. 1

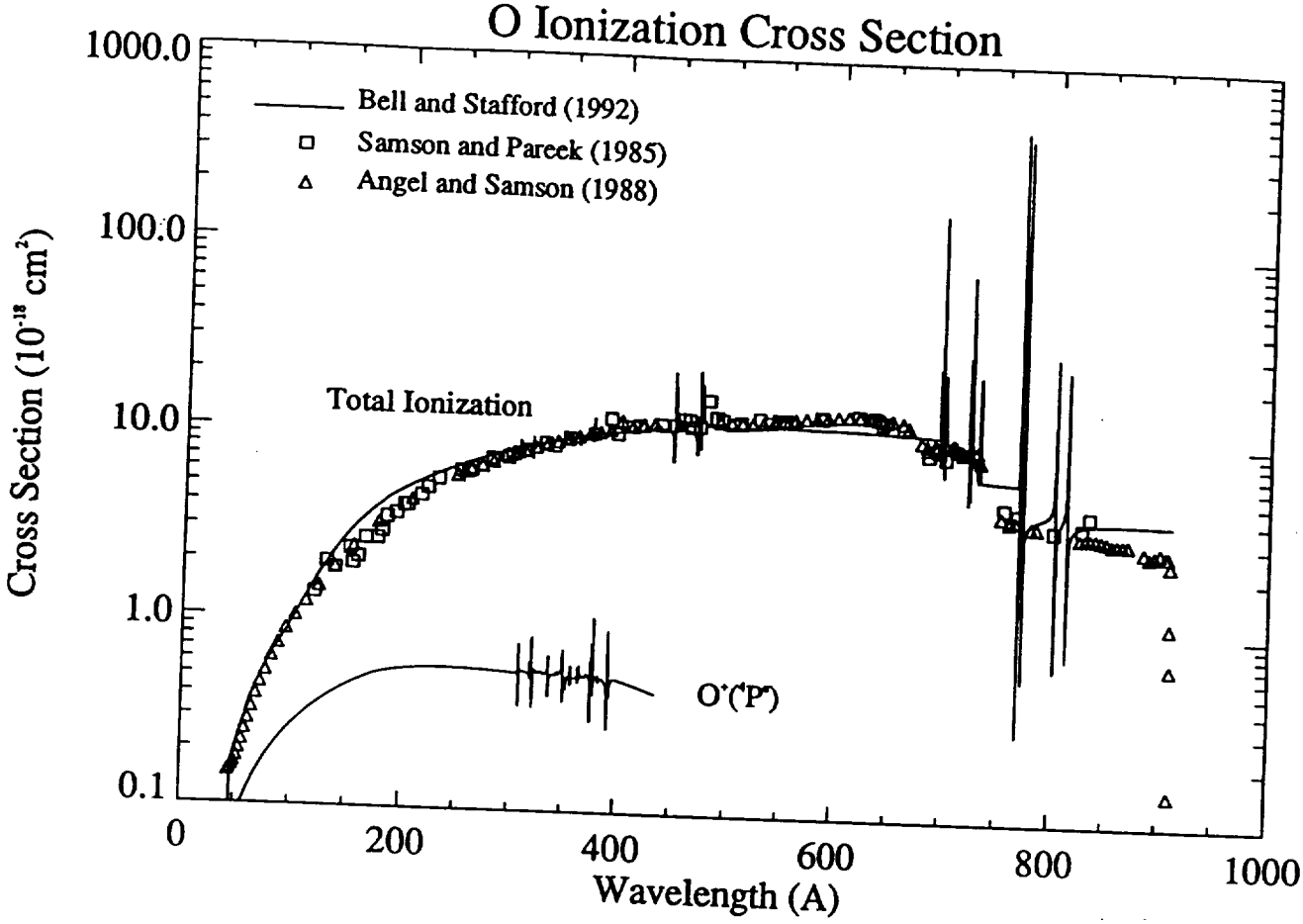
O Ionization Cross Section
Bell and Stafford (1992)
Samson and Pareek (1985)
Angel and Samson (1988)
Total Ionization
O+(4P)
Cross Section (10-18 cm2)
1000.0
100.0
10.0
1.0
0.1
0
200
400
600
800
1000
Wavelength (A)

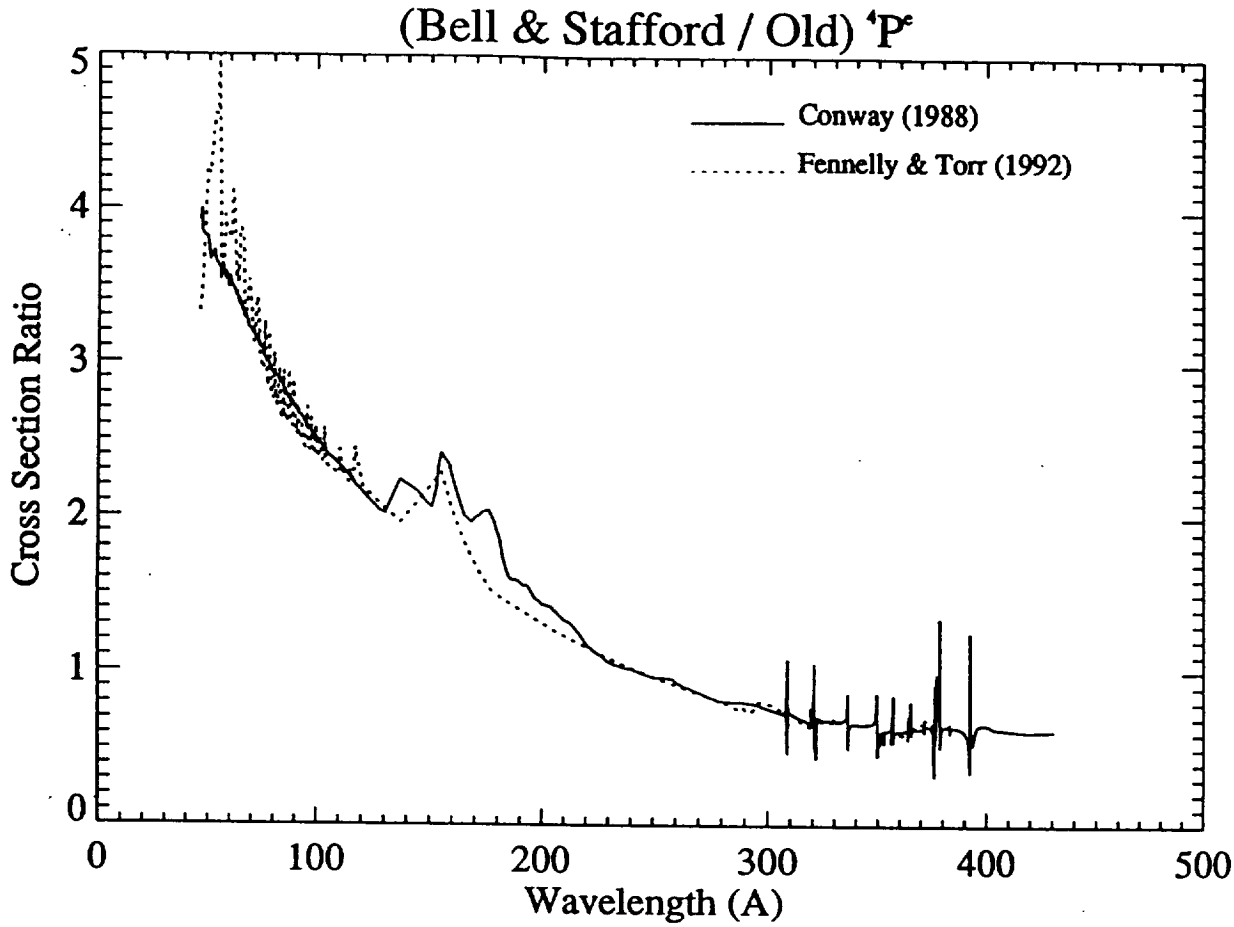
(Bell & Stafford / Old) $^4P^e$
Conway (1988)
Fennelly & Torr (1992)
Cross Section Ratio
Wavelength (A)
0
1
2
3
4
5
0
100
200
300
400
500

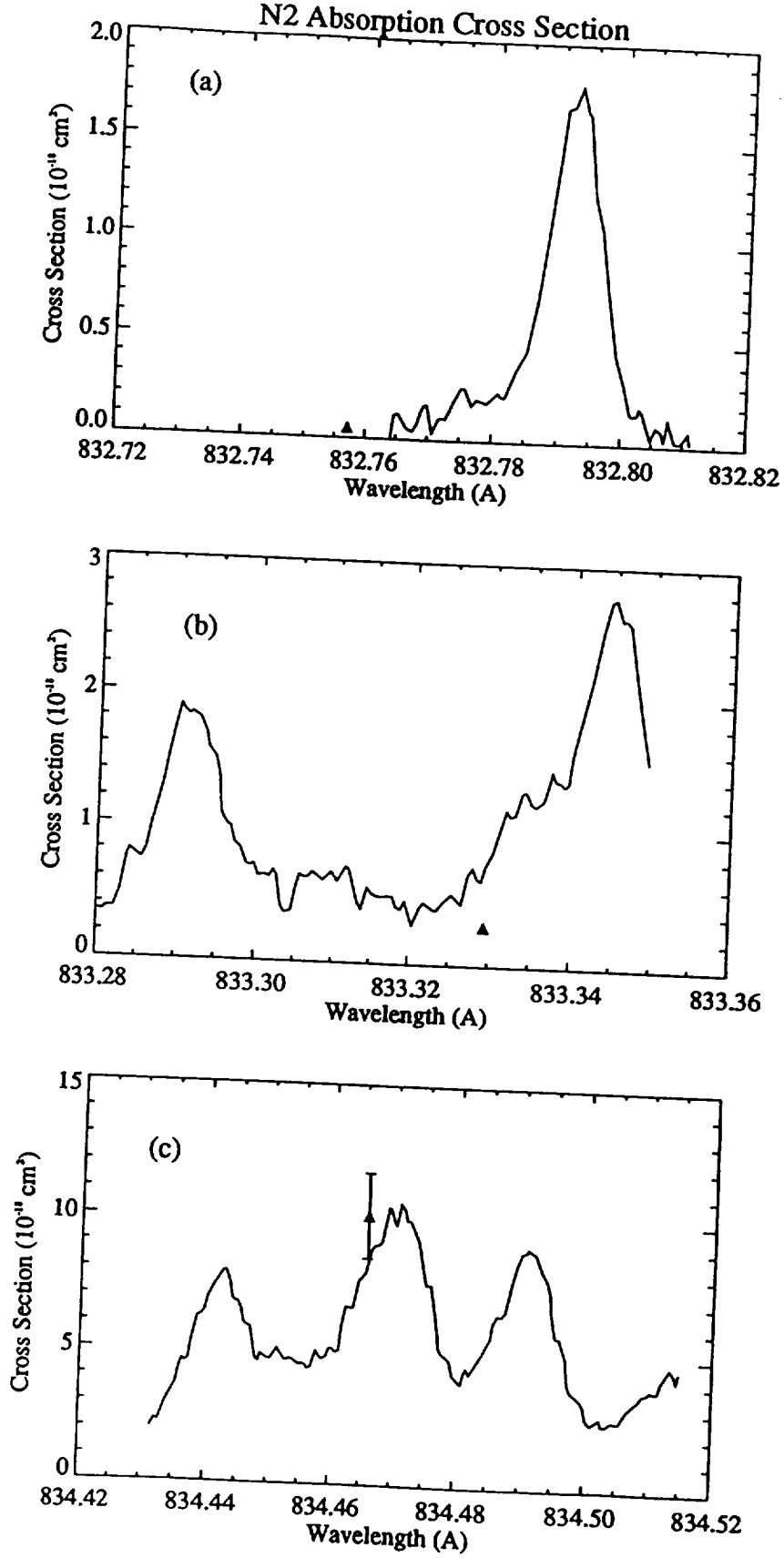
N2 Absorption Cross Section
(a)
Cross Section (10^{-18} cm^2)
2.0
1.5
1.0
0.5
0.0
832.72
832.74
832.76
832.78
832.80
832.82
Wavelength (A)
(b)
Cross Section (10^{-18} cm^2)
3
2
1
0
833.28
833.30
833.32
833.34
833.36
Wavelength (A)
(c)
Cross Section (10^{-18} cm^2)
15
10
5
0
834.42
834.44
834.46
834.48
834.50
834.52
Wavelength (A)

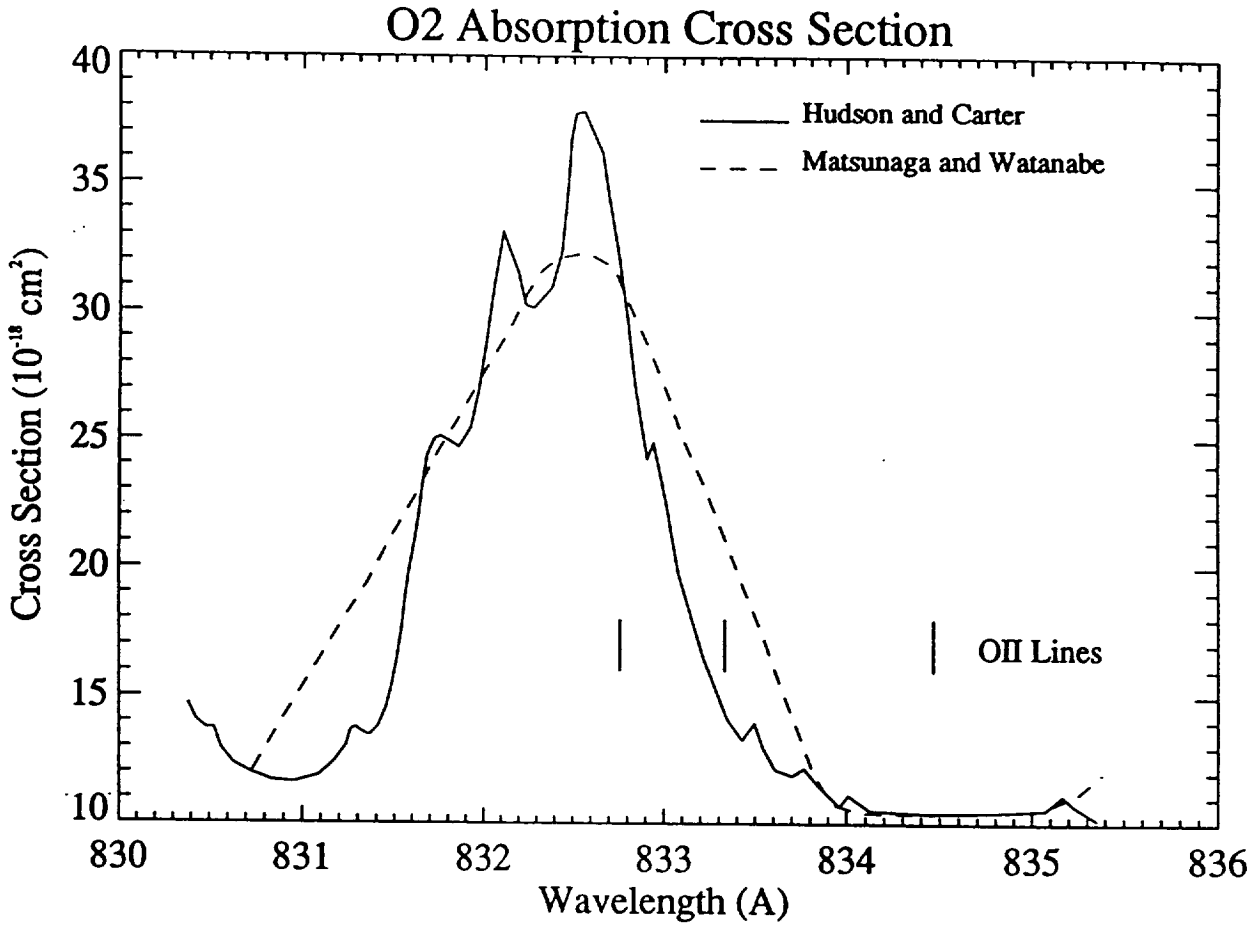
O2 Absorption Cross Section
Hudson and Carter
Matsunaga and Watanabe
OII Lines
Cross Section (10^{-18} cm^2)
Wavelength (A)
40
35
30
25
20
15
10
830
831
832
833
834
835
836

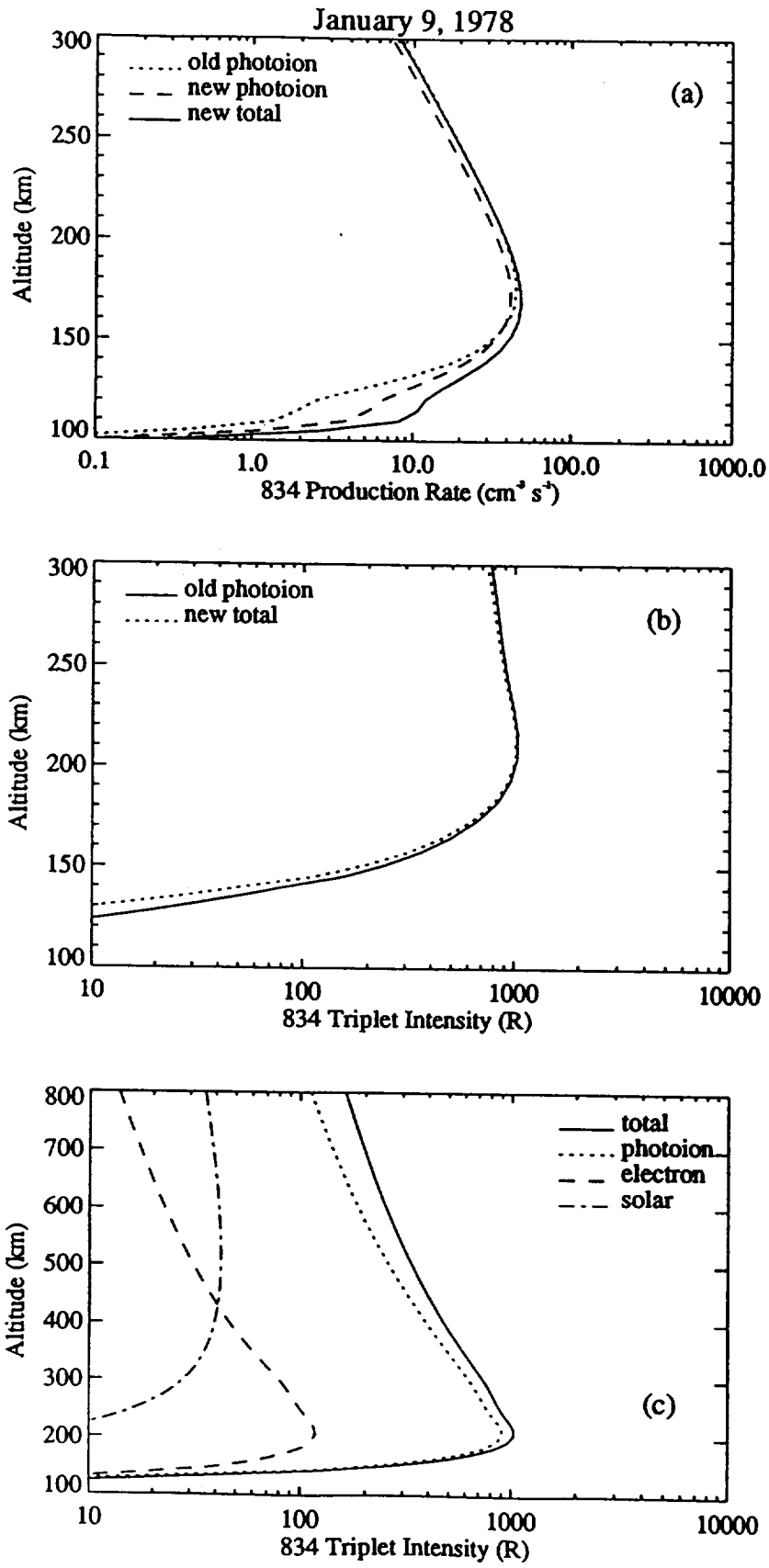
January 9, 1978
old photoion
new photoion
new total
(a)
Altitude (km)
834 Production Rate (cm⁻³ s⁻¹)
old photoion
new total
(b)
834 Triplet Intensity (R)
total
photoion
electron
solar
(c)

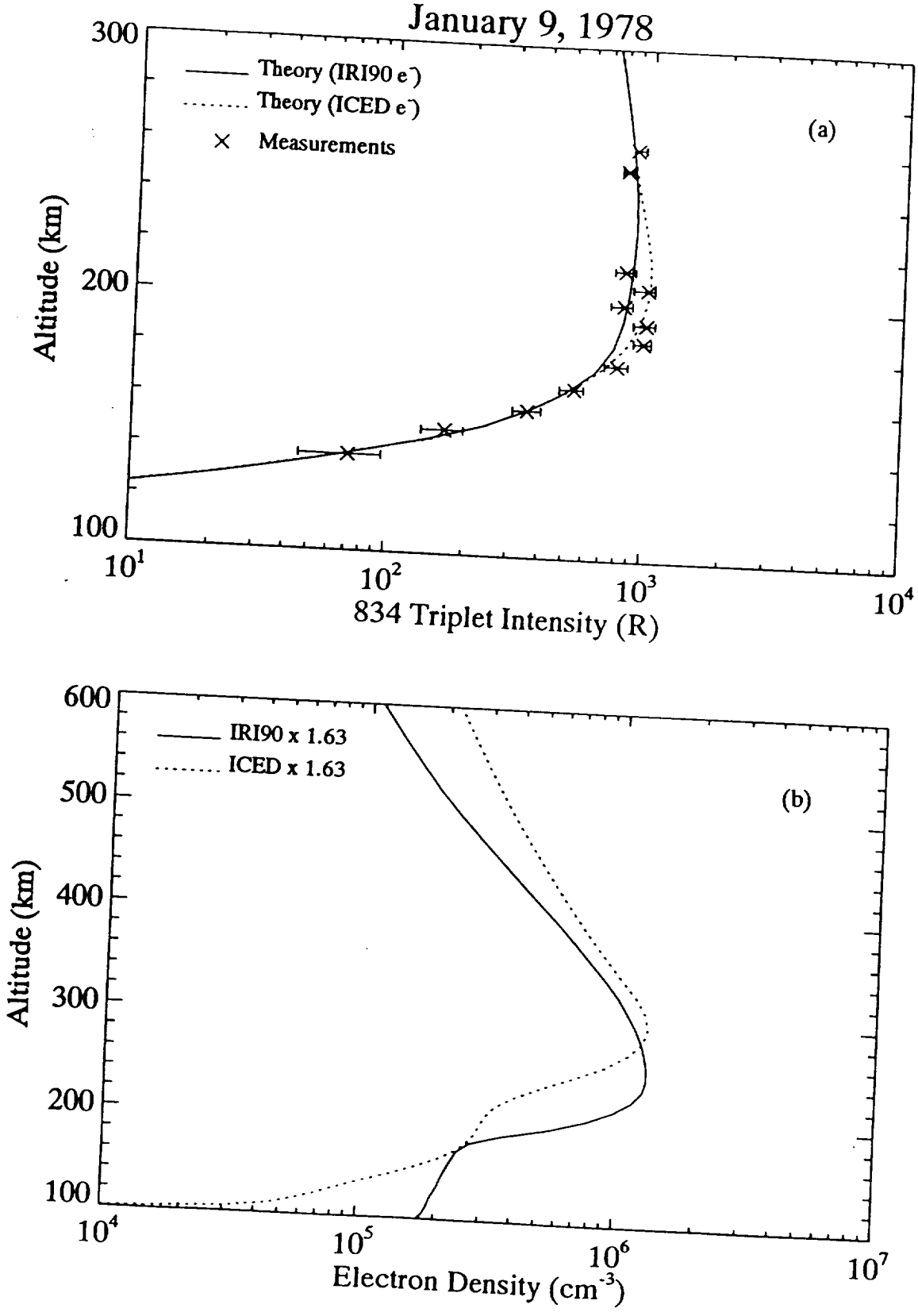
January 9, 1978
Theory (IRI90 e⁻)
Theory (ICED e⁻)
Measurements
(a)
Altitude (km)
300
200
100
10¹
10²
10³
10⁴
834 Triplet Intensity (R)
IRI90 x 1.63
ICED x 1.63
(b)
600
500
400
300
200
100
10⁴
10⁵
10⁶
10⁷
Electron Density (cm⁻³)

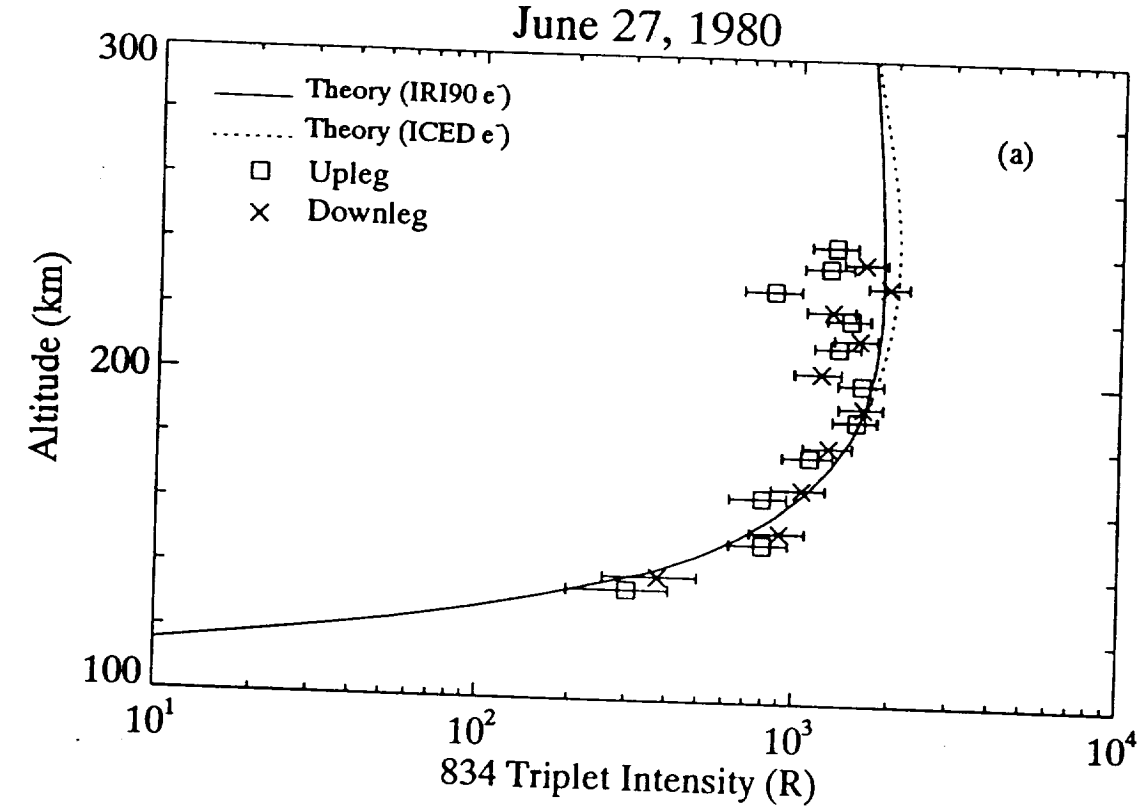
June 27, 1980
Theory (IRI90 e⁻)
Theory (ICED e⁻)
Upleg
Downleg
(a)
Altitude (km)
300
200
100
10¹
10²
10³
10⁴
834 Triplet Intensity (R)

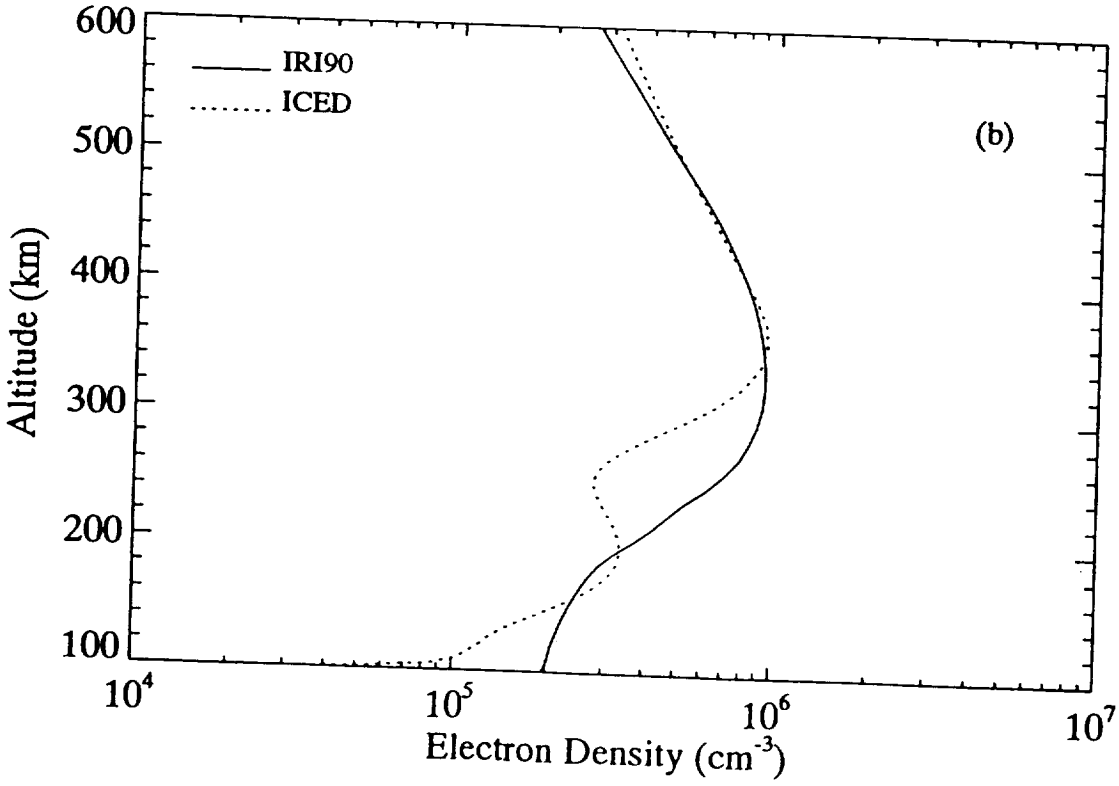
IRI90
ICED
(b)
Altitude (km)
600
500
400
300
200
100
10⁴
10⁵
10⁶
10⁷
Electron Density (cm⁻³)

APPENDIX B

On the Determination of Electron Densities Using O^+ 834-Å Emission

R. Link, J. S. Evans, and D. J. Strickland
Computational Physics, Inc.,
2750 Prosperity Avenue, Suite 600, Fairfax, VA 22031

G. R. Gladstone
Space Sciences Laboratory, University of California
Berkeley, CA 94720

Submitted to *Geophysical Research Letters*
March 23, 1993

Abstract. This study examines the problem of determining F-region electron densities from satellite limb scans of the O^+ 834-Å emission. It is shown that electron density profiles inferred from limb scans are not necessarily unique; estimates of N_mF_2 and h_mF_2 can vary by at least a factor of two and 50 km respectively.

Introduction

Link et al. [1993] examined the production of $O^+(2s^2\,2p^3\,{}^4S^o \leftarrow 2s\,2p^4\,{}^4P)$ 834-Å triplet emission in the dayglow. Using new calculations of O^+ partial photoionization cross sections [*Bell and Stafford*, 1992] and oscillator strengths (K. L. Bell, private communication, 1992), and a new laboratory measurement [*Morgan et al.* 1993], of the rotationally-resolved N_2 photoabsorption cross section near 834 Å, *Link et al.* [1993] obtained agreement with rocket measurements of the 834-Å emission in 1978 [*Gentieu et al.*, 1979] and 1980 [*Gentieu et al.*, 1984]. Using the ICED [*Tascione et al.*, 1988] and IRI-90 [*Bilitza*, 1990] empirical models to specify the ionospheric electron density (scaled upwards to match ionosonde measurements), *Link et al.* [1993] noted a lack of sensitivity to the adopted electron density profiles for the rockets viewing horizontally below 250 km. In this note, we explore the sensitivity of the 834-Å emission to the electron density profile for satellite viewing geometries.

Kumar et al. [1983] and *McCoy et al.* [1985] examined the dependence of the 834-

Å emission on the O^+ distribution, comparing their model results to 834-Å intensities measured by the STP78-1 satellite from 600 km altitude. Using analytic parameterizations of O^+ profiles, these studies investigated the sensitivity of the 834-Å emission to N_mF_2 (peak plasma density), h_mF_2 (peak altitude), and H_p (plasma scale height). Each parameter was varied individually, while the other two were kept fixed. *McCoy et al.* [1985] also considered the case of a 300 km orbit. *Meier* [1991, Section 5.2] updated the methodology using a newer photoionization cross section and a smaller total oscillator strength. Results were presented for a satellite altitude 850 km. These studies concluded that it is possible to infer the O^+ distribution from satellite zenith angle scans of the 834-Å intensity. We wish to point out that O^+ profiles determined in this manner are not necessarily unique.

Results and Discussion

Calculations are presented below for the two electron density profiles shown in Figure 1. We assume that the O^+ and electron densities are equal, a reasonable assumption in the F-region. The ICED curve (dotted line) is the same as that of *Link et al.* [1993] for the 1978 case, while the corresponding IRI-90 curve (solid line) has been arbitrarily adjusted in magnitude here for the sake of argument. The ICED and IRI-90 profiles peak at 300 and 250 km respectively, and differ in peak magnitude

by a factor of 2. The 834-Å excitation rates are those calculated by *Link et al.* [1993] for the 1978 rocket conditions ($F_{10.7} = 100.3$). Production of 834-Å emission by photoionization and photoelectron impact on atomic oxygen, and resonance scattering of solar 834-Å emission, are included in our model.

In Figure 2, we show 834-Å limb intensities calculated at four satellite altitudes using the electron density profiles of Figure 1. The tangent altitude scale here was selected to correspond to the zenith viewing angle range of 100° – 120° to be employed on an upcoming mission with an 850 km orbit. For this orbit, the computed limb intensity profiles are identical to within achievable calibration uncertainties, differing by less than 3% below 650 km. However, N_mF_2 and h_mF_2 differ by a factor of 2 and 50 km respectively. H_p also differs. The 600 km (STP78-1) orbit of Figure 2 fares little better. The $\leq$4% difference in the calculated limb profiles is well within the measurement uncertainty of the STP78-1 EUV spectrometer (see Figure 14 of *McCoy et al.* [1985]). The actual scatter in the STP78-1 data indicates that the uncertainties in derived electron densities will be worse than the factor of 2 found here for ideal noise-free profiles. The 450 and 300 km profiles are qualitatively similar. The maximum difference in limb profiles is about 5%. Note that the maximum tangent altitudes in this figure extend up to the observation point.

The same results are shown in Figure 3 for a wider range of look angles. For the 850 km orbit, the limb profiles differ above 105° due to the difference in scale height of the electron density profiles above 800 km. (The electron densities are extrapolated to infinity in our model). For the 600 and 450 km orbits, the uplooking limb profiles are very similar for ICED and IRI-90 cases. Most of the contribution to the 834-Å intensity comes from near the observation point where the ICED and IRI-90 electron densities are comparable. The 300 km orbit of Figure 3 shows perhaps the largest difference in shape of the limb profiles, but this difference is still $\leq$10% over the range of observing angles plotted. This large a difference is due to the fortuitous placement of the orbit at the peak of one of the profiles (ICED) of Figure 1, emphasizing the difference between the two. For the other altitudes, the location of the limb intensity peak differs little in Figures 2 and 3 for the two electron density profiles, although h_mF_2 differs by 50 km for these profiles.

The question arises of why the previous studies concluded that the 834-Å emission profile is a sensitive indicator of ionospheric electron densities. We believe that this is due to the fact that in these parametric studies, each parameter (h_mF_2, N_mF_2, H_p) was varied independently. In reality, these parameters are not independent. For example, the ionospheric response to variations in neutral exospheric temperature is changes in both peak altitude h_mF_2 and in scale height H_p. As h_mF_2 increases, so

does H_p, in general. Figures 91 and 93 of *Meier* [1991] show that the effects of these changes on 834-Å limb profiles largely cancel each other for zenith viewing angles greater than about 90° (downlooking). It is for this reason that the electron density profiles of Figure 1 produce such similar 834-Å limb profiles shown in Figure 2.

Finally, the previous studies cited above suggested that resonance scattering of solar 834-Å emission is a negligible source of airglow 834-Å emission. Our results (Figure 4) show that it may contribute up to about 27% of the uplooking 834-Å intensity for the 850 km orbit. Without simultaneous measurement of the O^+ solar 834-Å irradiance, it may be difficult to derive accurate electron density profiles from uplooking satellite 834-Å airglow measurements. The solar emission near 834 Å is a blend of O^+ and O^{++} multiplet lines, presenting additional complications [*Meier et al.*, 1991] which have been taken into account in the calculations presented here [*Link et al.* 1993].

Conclusions

The present results suggest that there may be difficulties in extracting a unique combination of (N_mF_2, h_mF_2, H_p) from 834-Å limb scans. In a realistic situation, experimenters must also contend with pointing errors, finite fields-of-view, calibration uncertainties, and statistical noise, suggesting that the uncertainties in the derived

$N_m F_2$ may even be larger than the factor of 2 found here. Our results also suggest that no matter how small the instrument field-of-view, even a 50 km difference in $h_m F_2$ cannot be resolved, at least for the two electron density profiles considered here. Any uncertainties in the 834-Å excitation source (the ionizing solar EUV irradiance, atomic oxygen abundance, solar O^+ 834-Å irradiance) or absorber densities (O_2, N_2) will exacerbate these problems. These potential sources of uncertainty have not been addressed in the available literature. Unfortunately, as shown by *Link et al.* [1993], rocket measurements will not provide a resolution to these problems.

The uncertainties in $h_m F_2$ and $N_m F_2$ may even be larger than estimated from the two profiles examined here; we have not examined any other profiles. However, it is clear from the results presented here that it may not be possible to obtain accurate ionospheric parameters ($h_m F_2$, $N_m F_2$, H_p) from measurements of 834-Å limb profiles.

Acknowledgements. This work was supported by NASA awards NASW-4744 (RL and JSE) and NAG5-1507 (GRG).

References

Bilitza, D., International Reference Ionosphere 1990, National Space Science Data Center, *NSSDCA/WDC-A-R&S 90-20*, Greenbelt, MD, 1990.

Bell, K. L., and R. P. Stafford, Photoionization cross sections for atomic oxygen, *Planet. Space Sci.*, *40*, 1419, 1992.

Gentieu, E. P., P. D. Feldman, and R. R. Meier, Spectroscopy of the extreme ultraviolet dayglow at 6.5-Å resolution: Atomic and ionic emissions between 530 and 1240 Å, *Geophys. Res. Lett.*, *6*, 325, 1979.

Gentieu, E. P., P. D. Feldman, R. W. Eastes, and A. B. Christensen, EUV airglow during active solar conditions 2. Emission between 530 and 930 Å, *J. Geophys. Res.*, *89*, 11,053, 1984.

Kumar, S., S. Chakrabarti, F. Paresce, and S. Bowyer, The O^+ 834-Å dayglow: Satellite observations and interpretation with a radiative transfer model, *J. Geophys. Res.*, *88*, 9271, 1983.

Link, R., J. S. Evans, and G. R. Gladstone, The O^+ 834-Å dayglow: Revised cross sections, *J. Geophys. Res.*, submitted, 1993.

McCoy, R. P., D. E. Anderson, Jr., and S. Chakrabarti, $F2$-region ion densities from analysis of O^+ 834 Å airglow: A parametric study and comparisons with satellite

data, *J. Geophys. Res.*, *90*, 12,257, 1985.

Meier, R. R., Ultraviolet spectroscopy and remote sensing of the upper atmosphere, *Space Sci. Revs.*, *58*, 1, 1991.

Meier, R. R., K. G. Widing, and U. Feldman, Analysis of the solar OI/OII multiplets at 834 Å: Implications for the emission measure distribution in the vicinity of 40,000 K, *Astrophys. J.*, *369*, 570, 1991.

Morgan, H. D., H. M. Seyoum, J. D. E. Fortna, D. C. Humm, A. Asfaw, and D. D. Cleary, Total photoabsorption cross section of molecular nitrogen near 83.4 nm, *J. Geophys. Res.*,, in press, 1993.

Tascione, T. F., H. W. Kroehl, R Creiger, J. W. Freeman, Jr., R. A. Wolf, R. W. Spiro, R. V. Hilmer, J. W. Shade, and B. A. Hausman, New ionospheric and magnetospheric specification models, *Radio Sci.*, *23*, 211, 1988.

List of Figures

Fig. 1 Electron density profiles used in the present study, scaled from the ICED and IRI-90 models (see text).

Fig. 2 Model 834-Å limb intensities at four altitudes. Tangent altitudes extend up to the observation point.

Fig. 3 Model 834-Å limb intensities at four altitudes, for zenith viewing angles of 70° – 120°.

Fig. 4 Contributions to the 834-Å limb intensity at an altitude of 850 km. Indicated are the photoionization plus photoelectron source (dotted curve), the solar scattering contribution (dashed curve), and total intensity (solid curve).

Fig. 1

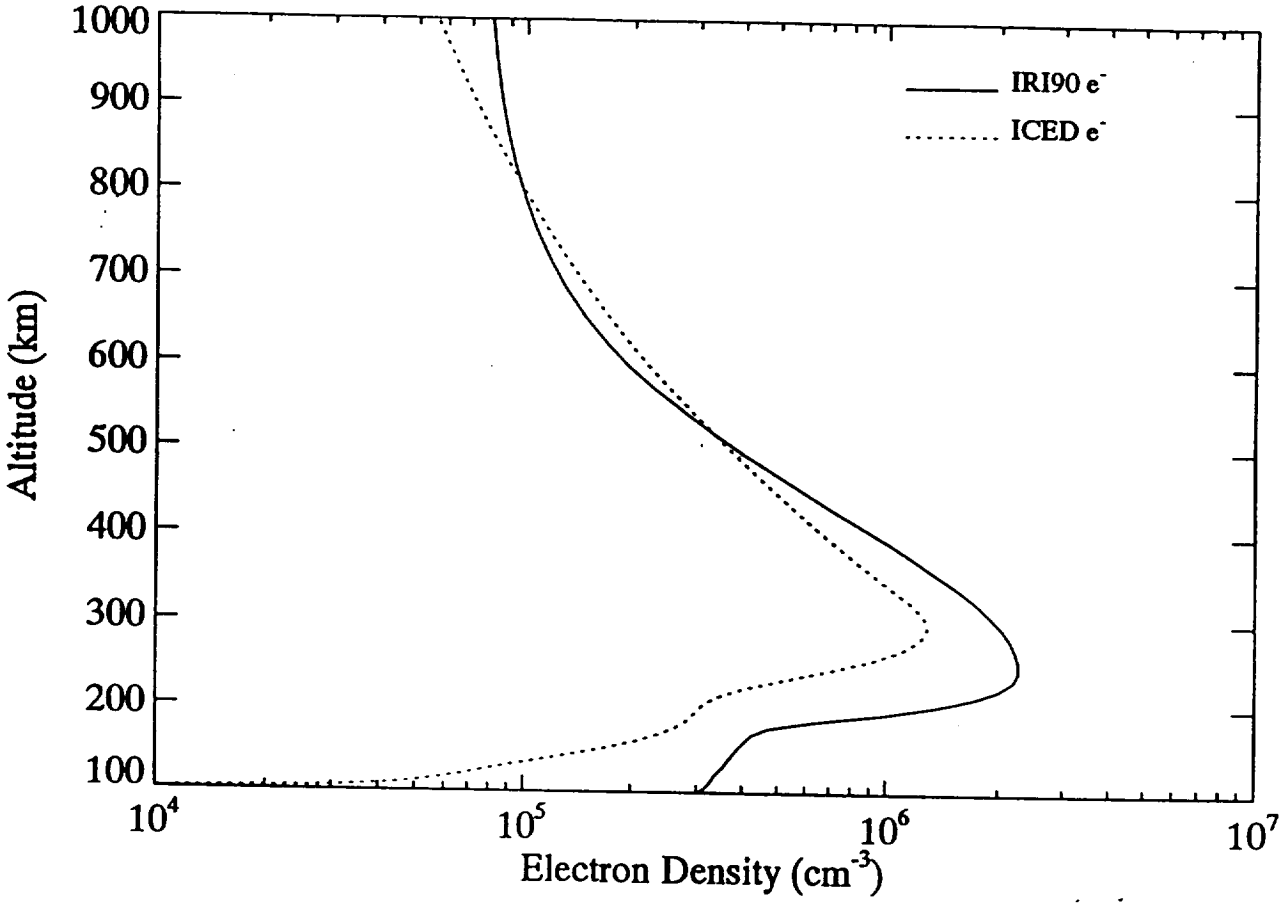
1000
900
800
700
600
500
400
300
200
100
Altitude (km)
IRI90 e⁻
ICED e⁻
10⁴
10⁵
10⁶
10⁷
Electron Density (cm⁻³)

Fig. 2

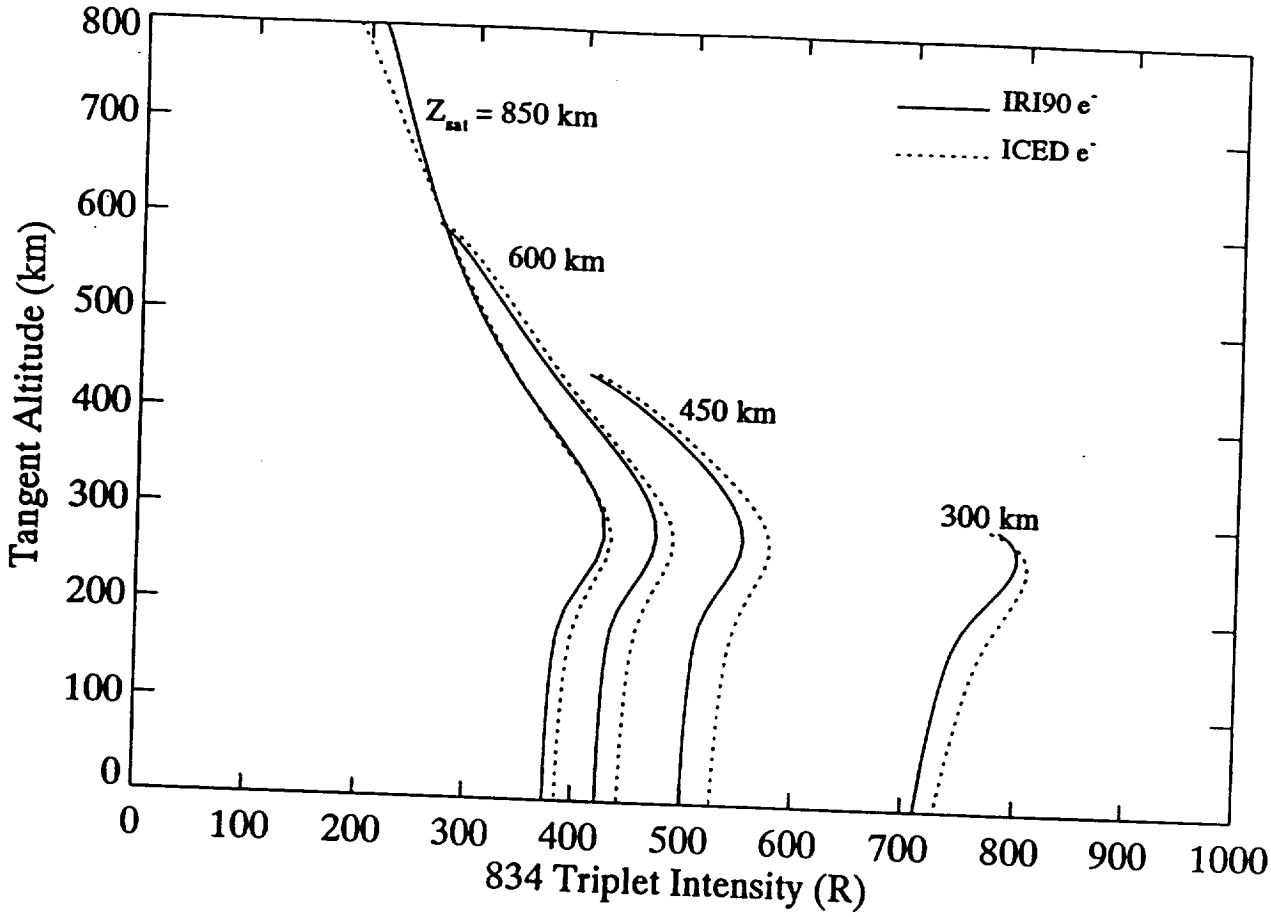
800
700
600
500
400
300
200
100
0
Tangent Altitude (km)
Z_{sat} = 850 km
600 km
450 km
300 km
IRI90 e⁻
ICED e⁻
0
100
200
300
400
500
600
700
800
900
1000
834 Triplet Intensity (R)

Fig. 3

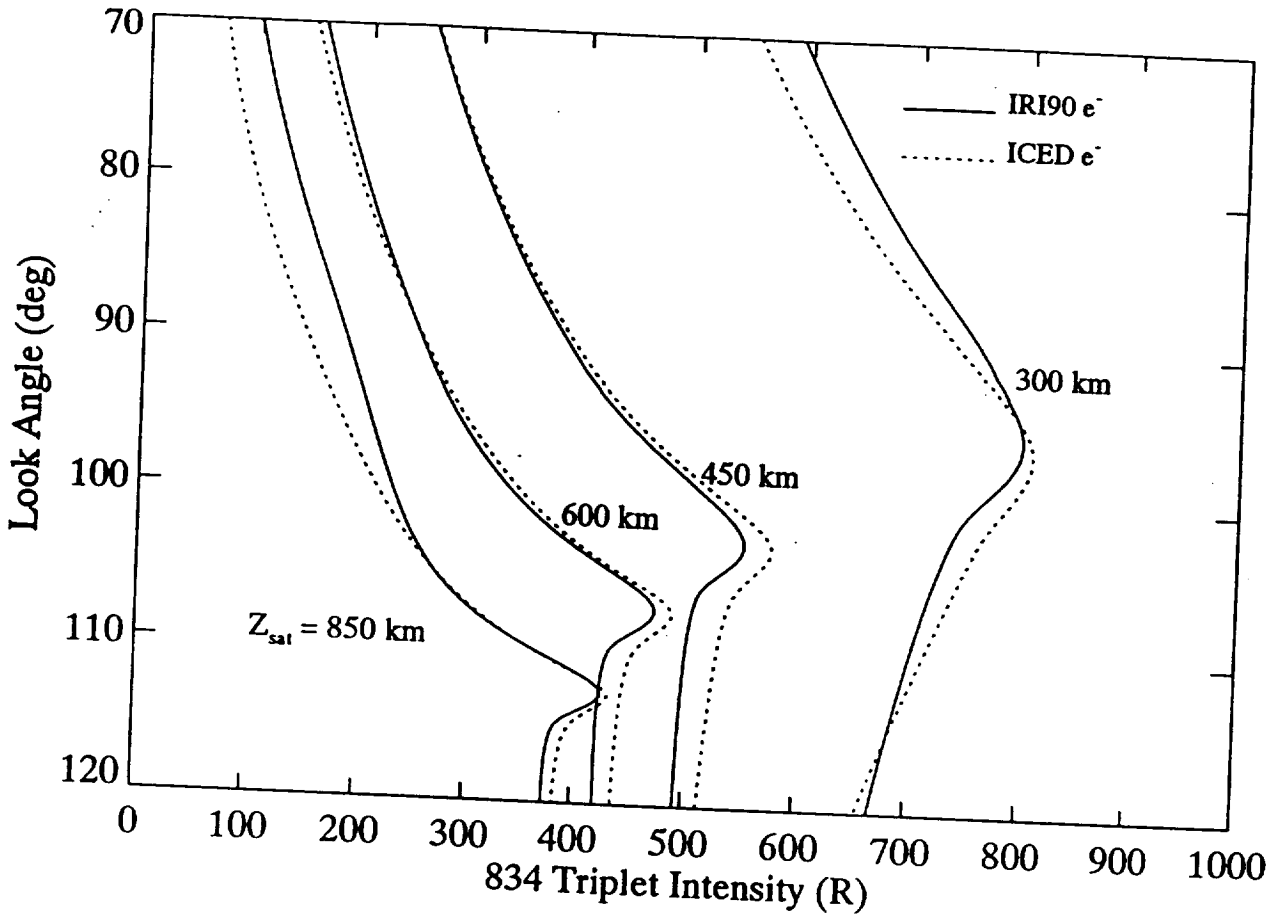
70
80
90
100
110
120
Look Angle (deg)
0
100
200
300
400
500
600
700
800
900
1000
834 Triplet Intensity (R)
IRI90 e⁻
ICED e⁻
300 km
450 km
600 km
Z_{sat} = 850 km

Fig. 4

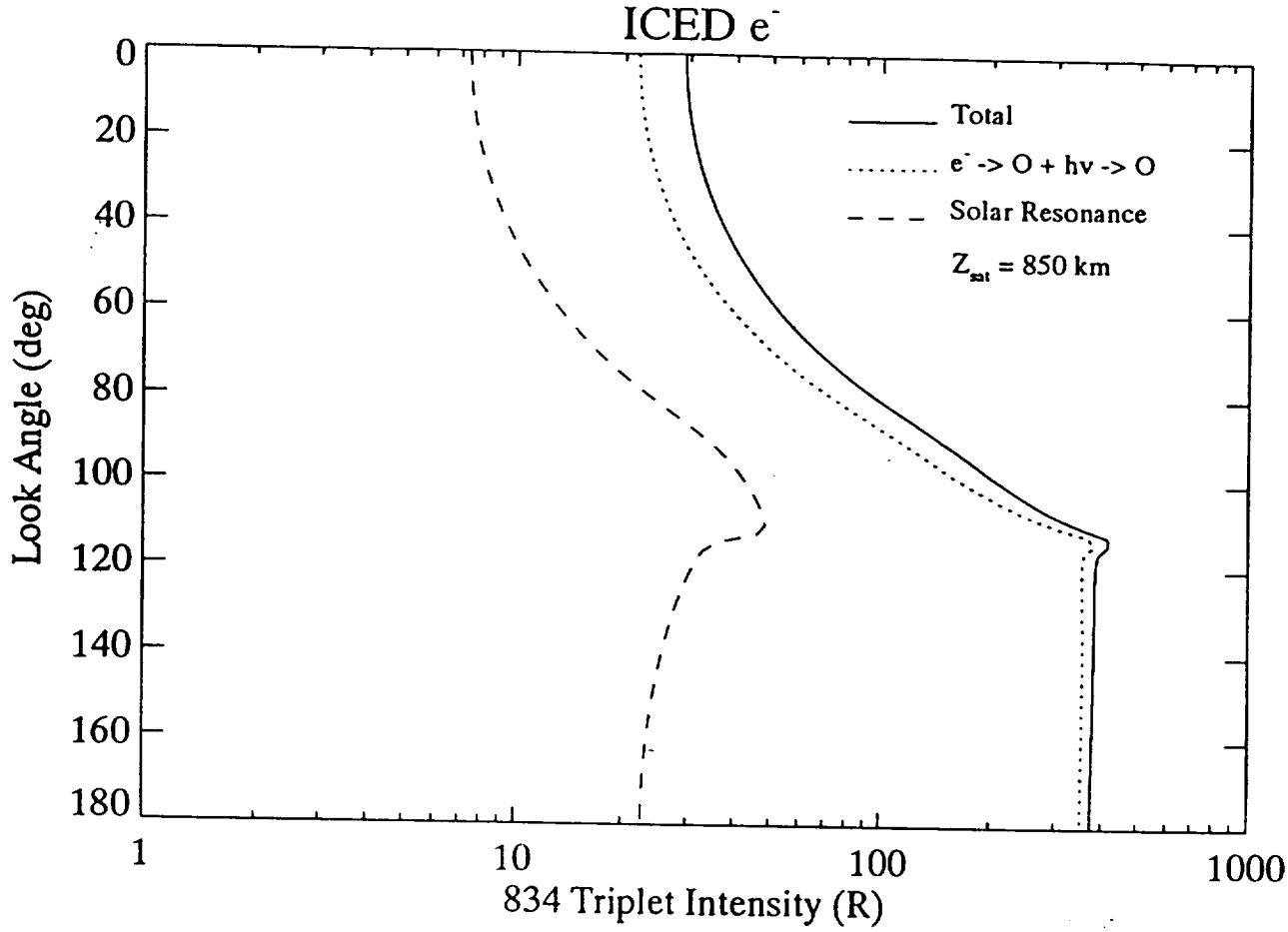
ICED e⁻
Total
e⁻ -> O + hv -> O
Solar Resonance
Z_sat = 850 km
Look Angle (deg)
0
20
40
60
80
100
120
140
160
180
1
10
100
1000
834 Triplet Intensity (R)